Ridging signatures in ~~high resolution~~ high-resolution SAR images

Mikko Lensu and Markku Similä

Finnish Meteorological Institute(FMI), Marine Research, Erik Palménin aukio 1, 00560 Helsinki, Finland

Correspondence: Mikko Lensu (mikko.lensu@fmi.fi)

Abstract. The statistics of ~~ice ridging signatures was~~ ice-ridging signatures were studied using high (1.25 m) and medium (20 m) resolution SAR images over the Baltic sea ice cover, acquired in 2016 and 2011, respectively. Ice surface profiles measured by the 2011 airborne campaign ~~was~~ were used as validation data. The images did not delineate well the individual ridges as linear features. This was assigned to the random occurrence of such ridge rubble arrangements that generate bright SAR ~~return~~returns. Instead, the ridging signatures were approached in terms of the local density of bright ~~pixels~~ returns selected by a ~~variable~~ variably bright pixel percentage (BPP). Density was quantified by counting bright pixel numbers (BPN) in pixel blocks with variable side length L. ~~As a sliding operation this resulted in enhanced ridging signatures and better applicability of SAR images in ice information production.~~ A statistical model for BPN distributions was determined by considering how the BPN values change with the BPP and was found to apply over a wide range of values for BPP and L. The statistical approach was also able to simulate a higher BPP image when seeded by a low BPP image. It was also found to apply to surface profile data analysed by counting ridge sail numbers in profile segments of variable length L. This provided a statistical connection between the bright pixel density and the ridge density. The connection was studied for the 2011 data in terms of surface rubble coverage estimated both from the ~~medium resolution~~ medium-resolution image and from the surface profiles. Apart from a scaling factor, both were found to follow the same distribution.

Keywords: sea ice, ice ridges, ridging parameters, Synthetic Aperture Radar (SAR), X-band, TerraSAR-X, statistical analysis, simulation.

1 Introduction

The ~~Baltic Sea is a semi-enclosed brackish sea water basin in northern Europe. Baltic drift ice has dynamic nature due to forcing by winds and currents, which results in an uneven broken ice field with distinct floes, leads and cracks, brash ice barriers, rafted ice and ice ridges. The upper limit for thermodynamically grown ice in the drift ice zone is 70 cm or less during most winters (Palosuo et al., 1982), while the keel depth of ice ridges is typically 5 to 15 m (Leppäranta and Hakala, 1992; Ronkainen et al., 2018)~~ .

~~Navigation in the Northern Baltic continues trough the ice season. During an average winter all Finnish ports become surrounded by ice and they~~ ports of the northern Baltic Sea are kept accessible by icebreakers during severe winters~~also. As there are annually up to 20,000 port calls trough the ice cover in Finland only,~~ , and there exists a demand for accurate

ice information~~especially on ridging conditions. Without the presence of ridged ice the managing of wintertime maritime operations would be much simpler matter.~~

~~Ridge fields complicate the navigation and icebreaker assistance by inducing performance variations between ships of different capabilities as well as speed variation for each individual ship. This includes occasional besetting , which, in convoy operations, increases collision risks and causes delays and disorder in port logistics. Better information about the distribution of ridged ice would improve routing, icebreaker operation planning and the predictability of arrival times. This would make the Baltic winter navigation system as a whole more efficient, safe, environmentally friendly and economical. This applies also to other to other ice infested sea areas.~~

~~Operative production of ice ridging information is based on satellite data and surface observations.~~ , especially on ice ridging. Ridge fields increase collision and besetting risks and reduce the predictability of shipping operations. In the Finnish-Swedish ice charts~~this information~~ , ridging is coded by the degree of ice ridging (DIR), which is a numeral ~~that seeks not only to quantify ridging but also to characterise navigational difficulty. Icebreakers communicate their estimates of DIR values to the ice services where DIR values are assigned to ice chart polygons using the estimates, other data,~~ based on icebreaker observations and manually interpreted SAR images.

Due to the qualitative nature of DIR~~the need for truly quantitative ridging statistics~~ , a need for SAR methods to retrieve quantitative ridging parameters persists. The usual surface parameters ~~to describe ridging are ridge~~ are ridge sail height and ridge density~~or the number of ridge sails per km along a linear track. The surface statistics can be linked to the statistics of the subsurface ridge keels with cross-sectional modelsfor sail and keel geometry. This provides estimate of the total mass of ridge rubble from the surface parameters. Statistical models can also be used generate simulated thickness profiles for ridged ice, applied to model ship speed reduction and besetting risk (Kuuliala et al., 2016). Finally, ridge~~ , which can be used to parameterise associated statistical models. Ridge sail height and ridge density are also related to the fraction of the surface area covered by ridge rubble, a parameter ~~which~~ that contributes to the magnitude of ~~σ^o~~ σ° in SAR images

~~Ridge sail height and density can be determined by airborne profiling measurements which however do not usually belong to the routines of ice information production. At the same time, research seeking to determine ridging parameters from SAR images has not made enough progress to fulfill the expectations of the ice information producers. This difficulty has three main sources. Individual ridges are usually not resolved, the characteristics of the satellite instruments, images and acquisitions are varying, and there are sensitivities to ambient conditions and surface properties not related to ridges. To this adds the fact that ground truth data and the SAR signatures cannot usually be matched if the ice has drifted or deformed in the meantime.~~

~~In this paper we approach the problem in a way that makes feasible the quantification of ridge density from SAR at least in a relative fashion. The approach relies on the assumption that ridge density variation dominates the spatial variation of ridging signature in SAR images. The same statistical model is found to apply both to the variation of ridge density and to the variation of density of pixels chosen to represent~~ . The surface statistics can be linked to the subsurface ridge keel statistics with cross-sectional models, providing an estimate of the total mass of ridged ice. ~~An extensive set of Baltic surface profile data is used to formulate and validate the statistical model for ridge density. Two different TerraSAR-X X-band SAR images from the Baltic Sea are used, obtained with different imaging modes and resolutions. The high resolution (1.25 m) image is~~

used to study how individual ridges contribute to SAR signatures, and develop the statistical model in SAR context. The other, with 20 m resolution, is nearly concurrent with the surface data set which is used to validate the approach.

2 Background

SAR-based retrieval of ridging has previously approached the problem SAR research has approached ridging from two main directions. Physics based approaches have tried based approaches seek to determine the microwave backscattering properties of ridged icetypes so that these could be distinguished from other ice types. The scale of this problem ranges from the size of ridge blocks to the pixel size of low resolution SAR images for which the ridged ice σ° comes from a mixture of block accumulations and other ice types. On the other hand, image based , while image -based approaches seek to develop methods to retrieve degrees of ridging using retrieve ridging with image segmentation methodologies, supported trained and validated by field data.

One reason for the weak connection between the physics based and image based approaches is that it is not well understood It is still not well-understood how the pixel-to-pixel intensity variations relate to the ridging statistics and how this is affected by different wavelengths, polarisations, viewing angles, platforms, resolutions, roughness types, and ambient conditionsvariation in ridging. Backscattering from rafted ice, brash, sastrugi and other rough surfaces rough surfaces like brash and sastrugi may overwhelm the ridging signaturesignatures, and changes in temperature, moisture and snow cover may alter the discernibilityof ridging signatures from day to day. Theoretical models, e. g., (Albert, 2012), predict that for high frequency waves the their discernibility. Air temperatures around 0 degrees reduce the penetration depth of microwaves into the snow layer, decreasing the backscattering. For high frequencies, volume backscattering may exceed surface backscattering and significantly change the σ°. A feature specific to (Albert, 2012). For low-salinity iceis the importance of scattering , the scattering is dominated by volume inhomogeneities in the uppermost part layers of the ice. As verified by (Dierking, 1999) this partly , which in part explains the high variation in of X-band σ° values for the northern Baltic Sea ice for which the salinity ranges from 0.2 to 2 permille (Hallikainen, 1992).

Not many papers have addressed the identification of ridges from SAR imagery. The likely reason is that the resolution of the operative SAR satellite modes has been too low, (Dierking, 1999). As the resolution of operative SAR data is usually not better than 100 m , to resolve individual ridges. Instead, the σ° depends on the aggregate effect of highly variable conditions in each pixel. For an experienced eye it may appear evident which texture typesindicate ridging even in very low resolution imagery. The step from this to quantitative methods has proved hard although correlations clearly exist. An article which discussed detecting ridges in length is (Melling, 1998) where the study area was in the Beaufort Sea. A strong correlation was observed between the spatial frequency of ridges identified from the SAR and the average draft of the ice field in the X-band. It was noted that the X-band airborne SAR (25 m resolution) yielded better ridge identification than the C-band ERS-1 SAR (30 m resolution) for first-year pack ice. values come from varying assemblages of ridge rubble and other surface types. Correlations between SAR signature and ridged ice volume emerge, as shown in the Beaufort Sea study of (Melling, 1998), but quantitative estimates are hard to obtain.

In the BalticSea the most intensive phase of the SAR based work related to sea ice ridging took place in late 1980's and early 1990's. Several aspects of the problem were examined. There were both physics based approaches seeking to model the microwave backscattering from ridges, and image based approaches trying to identify ridging signatures from SAR images or classifying them with respect to degrees of deformation. Backscattering models were constructed by (Johansson et al., 1992; Manninen, 199 . These included also three-dimensional models taking full ridge geometry in account, that is, the shape of the ridge sails and the size, shape and angle distributions of the sail blocks, physical backscattering was studied extensively in the 1980s and 1990s. This included models taking the sail block angle distributions into account. According to the 3D backscattering model for an ice ridge by (Manninen, 1992) 3D model of (Manninen, 1992, 1996), the most important ice properties in the C-band microwave surface backscattering from ridge sails are , in order of importance, backscattering from ridges are microscale surface roughness, dielectric constant and geometrical properties of the ice blocks. If the surface roughness and dielectric constant variations over the ridged and surrounding areas are small the magnitude of backscattering is dictated by the geometry of the ice block accumulations, basically the relative surface area covered by the accumulations and the orientations of the ice blocks in them.

In (Carlström and Ulander, 1995) the authors used 2D-model where an ice ridge is assumed to be a collection of circular facets with superimposed surface roughness. Thicknesses and slopes of facets varied. The authors concluded that the specular reflections are dominant unlike the results reported by (Manninen, 1992). According to (Manninen, 1992, 1996) the sail block geometry. The main difference between ridged and level ice is was that backscattering from ridge blocks has a broad range of incidence angles, whereas level ice has a very narrow range. On the other hand, using a 2D model describing the sail as a collection of circular facets with variable surface roughness, (Carlström and Ulander, 1995) concluded that specular reflections are dominant. Both models predict rather similar results for first-year ridges in C-band SAR imagery due to the broad distributions of ridge-block ridge block orientations and dimensions. Ridge backscatter has also been observed to be slightly sensitive to the radar azimuth angle by (Johansson et al., 1992). We note that the modelling predictions based on *in situ* measurements agreed well with SAR data in the comparison reported by (Carlström et al., 1997).

Due to the complicated nature of the geometric models they can hardly be utilised in practice to interpret observed σ°. Sufficient understanding of ridging statistics, required for the integrating the physical model for areally averaged backscattering values, has been lacking as well. However, the physical models help us understand which ice properties control the separation of ridges from the surrounding level ice and why ridges often remain undetected even in high resolution SAR images or fail to appear in them as continuous curvilinear features.

In our SAR based ridging studies we have often indicated the intensity of ridging using the degree of ice ridging (DIR) categories in the absence of field data for large sea ice areas. The DIR classes are semi-heuristic numerals although a clear correlation between the classes and deformed ice volume was found for the profile 2011 data set used in (Gegiuc et al., 2018) . The earliest SAR based ridging estimation in the Baltic Sea was (Similä et al., 1992) where a regression estimation for ridge density was proposed with Baltic image-based research has mostly used nonlinear regression and Bayesian methods to classify ridged ice types. (Similä et al., 1992) found reasonable results using surface profile data and tail-to-mean ratio as a predictor. Tail-to-mean ratio is a function of computed from the SAR pixel value distribution It yielded reasonable results for the test

set consisting of the *in situ* airborne profiling databut due to lack of further validation data the model could not be adapted to different ice conditions . Later, the DIR estimation problem in the Baltic Sea has been investigated in multiple papers. as a predictor. Utilising 3D scanner data, (Similä et al., 2010) demonstrated that in dry and cold ice conditions with thin snow cover, a correspondence between freeboard and C-band SAR can be found if the dominant ice thickness is known.

In (Mäkynen and Hallikainen, 2004) the σ°, distributions were computed for several ice deformation categories with different incidence angles utilising data collected during many Baltic Sea scatterometer field campaigns. The utilised deformation categories approximated the DIR classes and were determined using a video-based assessment. and incidence angles from scatterometer campaign data. Only small differences were noticed between the X- and C-band results or using or different polarisations with the exception of HV-polarization. The results agree with those obtained in (Eriksson et al., 2010). Part of the scatterometer data collected by Mäkynen was reanalysed using a This agrees with the results of (Eriksson et al., 2010) . The same scatterometer data was utilised in the hierarchical Bayesian model in (Similä et al., 2001)with improved DIR classification results.

In (Gegiuc et al., 2018) sea ice ridging was assessed using the DIR classes retrieved from ice charts covering the whole Gulf of Bothnia. The analysis had of (Similä et al., 2001). (Gegiuc et al., 2018) assessed automated determination of DIR numerals in three stages: segmentation of a SAR image, computing a feature vector to each segmentand then , and classifying the segments. Training data consisted of several ice charts. Different ice charts served as the validation data for the classification maps. The results were encouraging and the method will be transferred into operational use. Thus it is possible to improve regional ridging information by combining advanced methods with usual operative information production by expert analysts. The actual ridging statistics required for effective ice routing and for ice forecast model assimilation is not captured by the DIR classes however. Gulf of Bothnia DIR numerals from ice charts. In addition, a clear correlation between DIR numerals and deformed ice volume was demonstrated using surface profile data.

A case study by (Similä et al., 2010) showed that in dry and cold ice conditions with thin snow cover it was possible to find correspondence between freeboard and C-band SAR data in the Baltic Sea assuming that the dominant thickness of the regional level ice is known. The used field data was collected during the CryoVex-2005 campaign. A nonlinear regression model with three control variables, σ°, the dominant thickness of level ice, and a variable accounting the effect of the SAR incidence angle, was used. The predicted estimates by the model followed closely freeboard changes also in the ridged area.

2 Approach

Considering the task to quantify ridging from a SAR image it is assumed here that open water areas have been detected (Karvonen et al., 2005). It may also be assumed that the ice cover signature has been segmented by an algorithm or by an ice charting expert into types among which ridged ice is one and such that the segmentation excludes other rough types of non-ridged surface with very bright return. The present approach concentrates on the remaining task of quantifying ridging for the ridged ice.

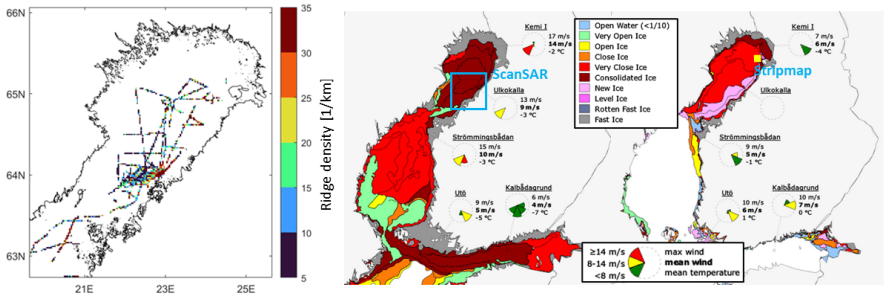

Figure 1. The profiling measurement lines during the 2011 field campaign.

In a birds-eye view ridging shows as block accumulations covering the surface. These are often identifiable curvilinear sails with approximately triangular cross section and with typical scale 1-10 m in across sail direction and tens to hundreds of meters in along sail direction. The essential feature of ridge rubble is that it may generate a strong backscattering signature. Thus all block accumulations with block structure resembling that of ridge sails are understood here as ridging. This includes rubble fields and other more chaotic block formations that cannot be decomposed into curvilinear sails. From backscattering viewpoint the the principal ridging quantity is the coverage (relative area) of ice surface covered by ridge rubble.

It appears clear that the returns from the ridge rubble dominate the brighter end of the backscattering intensity histogram. The brightness statistics involves certain uncertainty, however. The intensity histogram depends on the processing of the image and on enhancements aiming at good visual appearance. The ambient conditions affect the brightness statistics so that temporally separated SAR images from the same ridged ice field may have quite different intensity histograms. However, an ice charting expert could still recognise the same ridging features and would provide a similar manual classification to 'degrees of ridging' in both cases. This relies on observing that the order of intensity is retained by and large for the ridged ice types although the intensity histogram would change. The ridging signatures appear as persistent and symptomatically nonhomogeneous. This shows up clearly in binary images comprising a certain percentage of bright pixels from the intensity histogram tail. If the percentage is reduced, the ridging signatures become more sparse but tend to retain structural congruence with the non-reduced signatures.

In a way, the objective of the present approach is to provide statistical foundation for the assessment that the ridging signatures in two SAR images 'look the same'. Towards this end, a certain bright pixel percentage (BPP) is selected with an intensity threshold. For higher BPP the selected bright pixels are expected to be predominantly returns from ridge rubble. The spatial variation related to the ridging signatures is described in terms of the bright pixel number (BPN) in pixel blocks with side lenght L, or equivalently in terms of bright pixel coverage (relative area) in the blocks. The side length L and the BPP are variable parameters of the approach.

The results of this paper fall into two main categories. The first one presents application oriented results based on 'contextual images' obtained from a SAR image by a sliding BPN operation. The other one derives a model for the BPN statistics and seeks to validate it by observational data. Most proper validation data would consist of ridge rubble coverage in square areas

with comparable side length L. The extent of such data is limited, however. The validation data consists therefore of linear surface profiles from which ridge sails are identified. The profiles are divided into segments of length L and the ridge sail numbers (RSN) in the segments are counted. Only those sails are counted that exceed a certain height threshold.

Thus the BPN and RSN approaches are formally analogical and the the objective is to show that they follow the same statistical model. The model is derived by considering how BPN and RSN values change with threshold changes (threshold process). Ridge rubble coverage will inherit the RSN statistics that can then be parametrically compared with BPN statistics for concurrent datasets.

2 Data Sets and Processingmethods

2.1 SAR dataData

The German Two modes of TerraSAR-X (TSX) satellite was launched in 2007. It can be operated in different modes, usually in Stripmap or ScanSAR mode (Fritz and Eineder, 2013). The ScanSAR data were used. The medium -resolution HH-polarized ScanSAR image was acquired on 28 February 2011 over the northern part of the Sea of BothniaGulf of Bothnia. The high -resolution HH-polarized Stripmap image was acquired on 5 March 2016 near the Quark.It has swath width of Hailuoto island in the Bay of Bothnia. Surface profile data was collected in the Bay of Bothnia during 2 – 7 March 2011 along tracks shown in Fig. 1.

The ScanSAR swath width is 100 km and azimuthal length of the azimuthal length ofis 150 km. The ScanSAR mode consists of four Stripmap beams which are combined to achieve the 100 km wide swath.

The preprocessing of the ScanSAR image comprised calibration (calculation of σ°_{HH}), georectification and land masking., while in the studies, a 106x94 km subimage was used, Fig. 12. The image was rectified into the land masked and rectified to Mercator projection with 20 m pixel size. This georectification is compatible with the FIS ice charts and the navigation system of the Finnish and Swedish icebreakers. In this Mercator projection the reference latitude is reference latitude 61°40' N . The incidence angle varies and pixel size 20 m. As the incidence angle range from 29.5° to 38.7° . Because the incidence angle range is relatively narrow, we did not perform any statistical incidence angle correction is narrow, no incidence angle corrections were done, (Mäkynen et al., 2002), only the calibration of the backscattering coefficients σ°.

The equivalent number of looks (ENL) was on average 7 in the ScanSAR scene and the radiometric resolution 1.4 dB. The average noise equivalent sigma zero (NESZ) was -21 dB (Fritz and Eineder, 2013).

For high resolution SAR studies is used a Stripmap image acquired on 5 March 2016 near the Hailuoto island in the Bay of Bothnia . The acquired product Stripmap image is a Geocoded Ellipsoid Corrected (GEC) product without any terrain correction . It is also and a Spatially Enhanced Product (SE) designed for the highest possible square ground resolution. The HH-polarization image was rectified into 1.25 m resolution in the Mercator projection. The covered area is about $33.6 \times 42\text{km}^2$ (width $\times$ length). , from which a $19 \times 19\text{km}^2$ km subimage was used in the analyses, Fig. 2.

2.2 ~~Laser data~~

~~The laser data was collected during a helicopter-borne thickness profiling campaign in the Bay of Bothnia during 2 – 7 March 2011, i.e. ,~~ The ice profile dataset comprising 2800 km of the profile was collected during the week after the ~~acquisition of the ScanSAR image. The measurement system combines laser distance measurement to ice or snow surface and electromagnetic (EM) distance measurement to the ice–water interface. The measurement system~~ ScanSAR acquisition. The helicopter-borne system was similar to that described by (Haas et al., 2009). ~~The campaign comprises approximately 2800 km of helicopter-borne EM (HEM) measurement lines shown in Figure ??. After leaving the flight base the logging was turned on at about 64 N 23 E and within 50 km from this point the repeating tracks sample the ice cover almost completely in 1 NM resolution. Only the surface~~ Only the LIDAR surface profile data is used here~~. The thickness data~~ , while the electromagnetic (EM) ice thickness has been addressed in (Ronkainen et al., 2018)~~, and the relationship of the surface ridging parameters to the thickness and to the DIR ridging index of Finnish-Swedish ice charts in (Gegiuc et al., 2018).~~

~~The profiling measurement lines during the 2011 field campaign.~~

. The analysis of ~~laser~~ LIDAR data followed standard procedures~~described in (Eicken et al., 2009). The zero level was determined by conducting a two-step high-pass filtering with minimum point selection between the steps. Then~~ . After a reference-level determination, the local maxima were identified by ~~Rayleigh criterion demanding that~~ the Rayleigh criterion that demands that for two successive maxima, the minimum elevation between them must be less than half from either maximum. Otherwise, the shallower one is not counted. The elevation distribution of ~~Rayleigh separated maxima has~~ maxima has a negative exponential tail for values higher than 0.4 m~~that~~ , which was selected as ~~cutoff elevation.~~ the cutoff elevation, Fig. 1. Above the cutoff, the maxima are assumed to be ~~predominantly~~ ridge sails. The average ~~ridge height and density~~ sail height and ridge densities are 0.65 m and 11.7 1/km, respectively.

2.2 ~~Weather and Ice Conditions~~

2.1.1 ~~Winter 2010/2011~~

~~The winter 2010/2011 prior the field~~ The winter prior to the ScanSAR acquisition and profiling campaign was colder than average. ~~When the field campaignto the Bay of Bothnia started in late February, the the ice extent was larger than average annual maximum extent. There was a drifting ice station in the southern part of the basin from 25 February to 4 March (initial location 63°45.85' N,l21°55.34' E) after which the helicopter campaign continued to 7 March. During this period the Bay of Bothnia did not have 100% ice concentration because high SW winds , the mean wind speed being 10 m/s with variation from 5 m/s~~ During the campaign, SW winds up to 18 m/s ~~, repeatedly triggered drift~~ triggered opening and deformation periods ~~and opening in the southern part of~~ in the ~~basin. The wind direction changed NW during the helicopter campaign . According to the Finnish Ice Service ice charts the level ice thickness near the coast~~ Bay of Bothnia, and the drift speed of the research vessel Aranda serving as the campaign base was typically 0.1–0.4 knots. The ice thickness varied from 30 to ~~70 cm and from 30 to~~ 60 cm in ~~the middle of the Sea of Bothnia. The modal thicknesses of the HEM profiles are mostly within this range as well.~~

~~The air temperature began to increase from below~~ pack ice. The air temperature increased from -10 C° ~~(~~on 24 February ~~)~~ to -1.5 C° ~~(~~on 27 February~~)~~. When the ~~TSX~~ ScanSAR image was acquired, T_a was -2.3 C° ~~in the ice station.~~

~~Short snow lines were measured during 2-4 March . The mean thickness was~~ at the Aranda base. Snow lines measured during 2–4 March had a mean thickness of 8 cm and ~~the standard deviation (STD)~~ a standard deviation of 11 cm. About 50 ~~cm thick~~ cm-thick snow accumulations were often found by ridges, sometimes covering ~~the ridge sail~~shallower sails. On 3 March~~the snow had already some moisture~~ , the snow already had some moisture, and the density varied from 0.2 ~~-0.3~~to .3 kg/m3 on level ice and 0.3-0.4 kg/m3 near ice ridges. ~~We can assume~~ It can be assumed that during the ~~TSX image acquisition the~~ ScanSAR acquisition prior to the campaign, the snow was still dry and ~~it did not affect significantly~~ did not significantly affect the backscattering.

The ~~ice station drifted about 0.1-0.4 knots during the time gap between the TSX image and the helicopter flights. Throughout this time period additional deformation occurred in the area where the flights were performed. Hence neither the location nor the deformation characteristics of ridge fields stayed as they were at the time of TSX image acquisition. When assessing the results, these changes must be taken into account.~~

2.1.1 ~~Winter 2015/2016~~

~~The winter in~~ winter of 2016 was mild, and only the Bay of Bothnia had an ice concentration of 100%. Recurrent periods of mostly SW winds induced cycles of deformation, opening and ~~freezeup and only~~ freeze-up. Only in the beginning of March ~~the basin attained~~ did the basin attain a more persistent ice cover consisting of ridged and rafted ice types. On 5 March, the fast ice thickness in the NE quadrant of the basin was ~~50-65~~50–65 cm, the level of ice thickness in the ridged ice pack was 30-50 cm ~~,~~ and the air temperature was from -1 to ~~-4~~ 4 degrees. The temperature stayed below zero, and no snowfall occurred during the 10 days before the Stripmap SAR image acquisition date ~~,~~ when the snow thickness on ~~mainland being~~ the mainland was about 30 cm.

3 ~~High resolution SAR image analysis~~

2.1 ~~Ridging signatures and contextual images~~

~~The pixel size of the Stripmap image is 1.25 m which resolves backscattering signatures from individual ridges. The full image (Fig H1) size is 19x19 km but for analysis and visualisation we used also different subimages, principally 7000x7000 (8.7x8.7 km) and 1024x1024 subimages with representative ridging signature.~~

~~For better visualisation, images are also presented as category images for which the highest 30% of bright pixels is divided into three~~

2.1 Approach

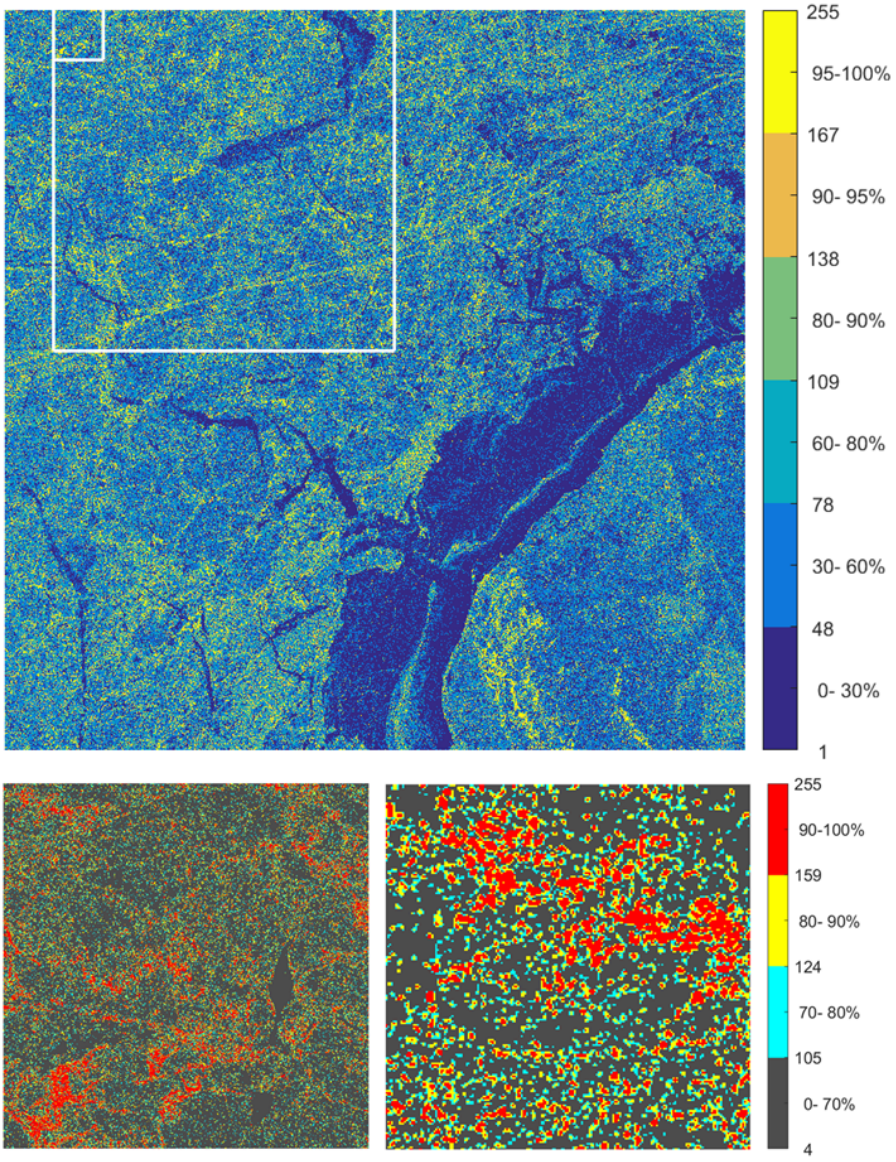

Figure 2. Full high-resolution Stripmap image with the 7000x7000 and 1024x1024 subimages indicated (upper panel). The 1024x1024 subimage and further 200x200 closeup from the upper left corner (lower panel).

From the backscattering viewpoint, the principal quantity to describe ridging is the relative area of ice surface covered by ridge rubble (rubble coverage). Curvilinear ridge sails are often visible, having a roughly triangular cross-section and a typical scale of 1–10 ~~% classes. In the 1024x1024 subimage ridging features appear then as delineated by the brightest 20 percent while the interval 70-80% begins to add more scattered pixels. The percentiles were 105 (-17.7 dB)for 70% , 124 (-15.5 dB) for 80%,~~

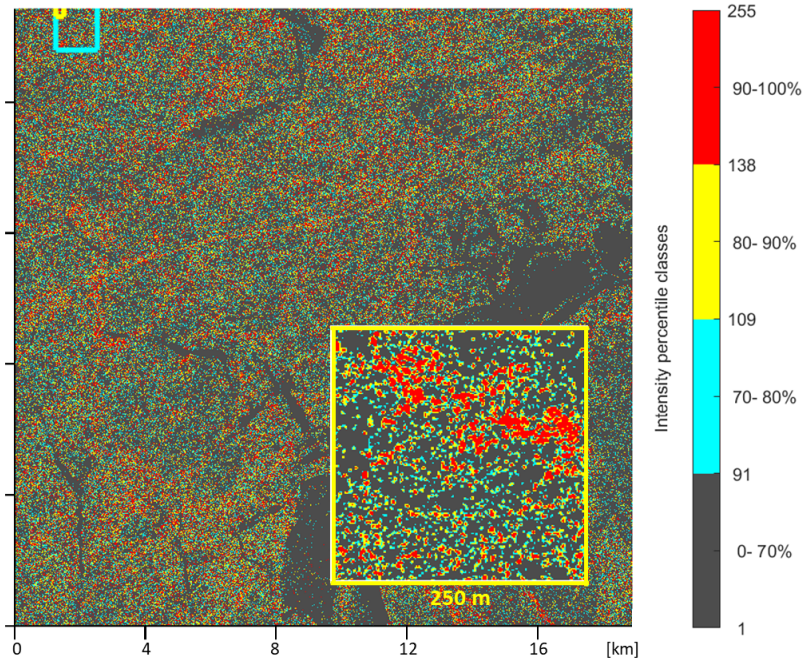

Figure 3. The categorised Stripmap 1024x1024 subimage and further 200x200 closeup from the upper left corner (lower right image).

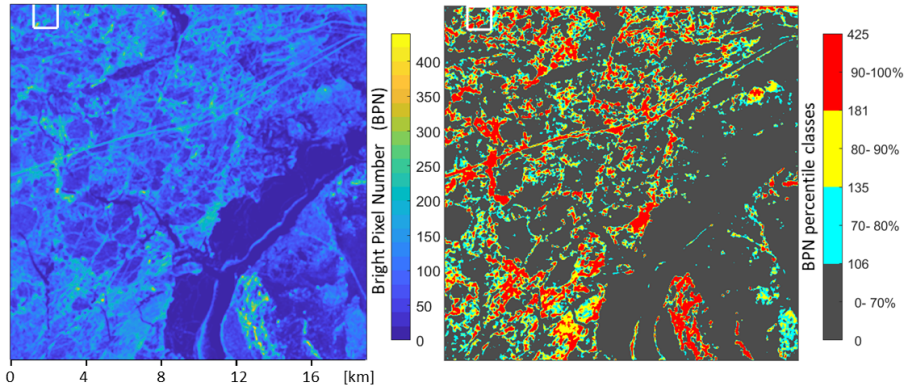

Figure 4. ~~Full high resolution Stripmap~~ The contextual images and corresponding category images derived from the full image with ~~the 7000x7000~~ BPP 20% and ~~1024x1024 subimages indicated~~ L=121 (upper panel)~~. The 1024x1024 subimage~~ , and ~~further 200x200 closeup~~ from the ~~upper left corner~~ 1024x1024 subimage with BPP 20% and L=21 (~~Lower panel~~lower panels).

~~and 159 (-11.3 dB) for 90%. It is seen that the hope of a similar quasi-photorealistic appearance as is found in comparable TerraSAR-X terrestrial images by Dumitru and Datcu (2013) fails to materialise. There are obvious linear ridges but these consist of chains of detached bright components that do not connect into continuous features. Larger features, reminiscent~~

of ridge groups or small rubble fields, are more readily observed . However, they are also aggregates of detatched bright components, with a texture not much different from ship channels that can be assumed to be flat and have uniform spatial distribution of bright scatterers. Increasing the bright pixel percentage from 30% improves slightly the connectedness of ridge signatures but at the same time obscures their delineation by adding scattered bright pixels in betweenm in the across sail direction and tens to hundreds of metres in along sail direction. However, less well-defined block accumulations are also understood here as ridging as they contribute to the rubble coverage. Their signatures in surface profiles are also similar to those of curvilinear ridges.

The contextual images and corresponding category images derived from the full image with BPP 20% and L=121 (upper panel), and from the 1024x1024 subimage with BPP 20% and L=21 (lower panels).

These observations agree with the results by Manninen (1992) and Carlström and Ulander (1995) indicating that bright returns from ridge rubble depend on random factors like favorable orientation of blocks while the returns from the remaining sail may fail to be clearly distinct from the surrounding level ice It appears clear that the returns from the ridge rubble dominate the brighter end of the backscattering intensity histogram. The brightness statistics involve a certain uncertainty, however. The histogram depends on the processing of the image aimed at a good visual appearance. A change in ambient conditions may result in quite different intensity histograms for an otherwise unchanged ice cover. Still, an ice charting expert can typically recognise in both cases the same ridging signatures as these appear persistent and symptomatically nonhomogeneous. The persistence shows up clearly in binary images comprising a certain percentage of bright pixels from the intensity histogram tail. If the percentage is reduced, the ridging signatures become more sparse but tend to retain structural congruence with the non-reduced signatures. The apparent randomness also corroborates the assumption that the density of the bright pixels in the image is proportional to coverage of ridge rubble and may act as proxy of ridge rubble coverage and ridge density.

To proceed following the approach outlined in Section 2.1In a way, the objective of the present approach is to provide a statistical foundation for the assessment that the ridging signatures in two SAR images 'look the same'. Towards this end, a certain bright pixel percentage (BPP) is selected and a binary image with unit values for the bright pixels is generated. The variation of bright pixel density with an intensity threshold. For a higher BPP, the selected bright pixels are expected to be predominantly returns from ridge rubble. The spatial variation related to the ridging signatures is described in terms of densities the bright pixel number (BPN) in pixel blocks with variable side length Lside length L, or equivalently in terms of bright pixel numbers (BPNthe bright pixel coverage (relative area, density) in the blocks. This is done as a sliding operation for the binary image, accomplished by a convolution with LxL unit matrix kernel. The result is 'contextual image' with the same size as the original image. The side length L and the BPP are variable parameters of the BPN approach.

Suggested by Figure **??**, the BPP is chosen to be 20%. The block side lenghts $L = 21$ (26 m) and $L = 101$ (126 m) are selected for the 1024x1024 and full images respectively. They are also shown as categorised images where the 30% of highest BPN values are divided into three 10% classes. It is seen that the ridging signatures are enhanced and their connectedness is improved in the contextual images (Figure **??**).

Including a pragmatic viewpoint, $L = 21$ and $L = 101$ correspond to the width and length scales of icebreaking ships so that the BPN values of contextual images provide the number of bright scatterers the ship bow or the whole ship interacts at a

time. If the BPN is accepted as a proxy of ridge rubble coverage, the contextual image has direct pertinence to the navigability. Efficient ship route optimisation in ridged ice cover is based on physical models for the added resistance from the ridges. The ice-going speed and the probability of besetting can then be obtained in simulations that take the iceconditions along alternative tracks as input (Kuuliala et al., 2016). The contextual image has potential to provide data for the purpose. The other possibility is to use ships' remotely observed response to classify the contextual image signatures in terms of ice cover resistance (Similä and Lensu, 2018). The classes of categorised contextual images can be interpreted as classes of navigational difficulty, or rather as delineation of areas that a ship should not enter. They can be used in tactical navigation or in route optimisation that only seeks avoid difficult ice types.

2.2 Sensitivity of contextual images

The pixel block side Proper validation data for the BPN approach would consist of ridge rubble topography in square areas with a comparable side length, for example, scanning LIDAR data over snow-free ice. The extent of such data is limited, however. The validation data, therefore, consists of linear surface profiles from which ridge sails are identified. The profiles are divided into segments of length L, and the ridge sail numbers (RSN) in the segments are counted. Only those sails are counted that exceed a certain height threshold. The ridge rubble coverage will inherit the RSN statistics that can then be parametrically compared with BPN statistics for concurrent datasets. The segment length L affects the resolution of detail in the contextual images and its value may be chosen to suit the context; hence the term. The question on the effect of BPP to the contextual images is of importance. There are also alternative methods to generate a contextual image, like sliding block average for intensity. With increasing BPP the variation of the BPN in the contextual image, measured by the coefficient of variation, decreases towards zero and the contrast between ridged areas and the background grows weaker. However, this appears less in the categorised images. Choosing BPP from the range from 2% (pixels with value 255) to 95% results into a catergorised images that are not much different from that in Figure **??**. This is also found if sliding intensity average is usedinstead. More strikingly, the information of the contextual image is essentially retained in different randomising transformations done for the original image. In Figure **??** the 1024x1024 image has been multiplied eight times by a random matrix which erodes the ridging signature of and the sail height threshold are variables of the original image almost beyond recognition. However, the contextual images still emerge essentially unchanged in their main features. RSN approach.

Results for 1024x1024 image multiplied 8 times by a random matrix. A) The 200x200 subimage B) Contextual image obtained by BPP 20% and 21x21 convolution kernel C) Categorisation in terms of coverage. As the BPN and RSN approaches are formally analogical, a more theoretical validation exercise seeks to show that they follow the same statistical model. The model is derived by considering how BPN and RSN values change with threshold changes (threshold process). High-resolution (1.25 m) images resolving individual ridge sails are used.

These observations indicate that, within the considered pixel block methods using the same block size, the order of the BPN values is only weakly affected by method change. For

2.2 Estimating ridge rubble coverage

Ridge rubble coverage can be estimated along a linear profile from ridge sail height and ridge density. To provide realistic estimates, the effect of the cutoff sail height used in the ~~10% classes used in the categorised images the change does not induce extensive flux of contextual image values across class boundaries. In more detail, starting with some reference method it can be investigated how the contextual image values are mapped to those of an alternative method. For example, mapping for $L = 21$ and BPP 20% the 1024x1024 image BPN values to matching $L = 21$ sliding intensity averages the relationship is monotonous on the average. For each BPN value the mapped intensity averages have a normal distribution with standard deviation in the range 3.5-4.5. On the other hand, the widths of the $70\% - 80\%$, $80\% - 90\%$ and $90\% - 100\%$ categories for the intensity average image are 9, 15~~ profile analysis must be assessed, as well as the application of results reported on the sail $width/height$ ratio, which is noted as $R = w/h$. Considering first the ridge width, the effect of oblique angles of sail crossings must be taken into account. For randomly oriented ridges, the average width is $\pi/2$ times the perpendicular width (Mock, 1972). The reported R ratios for perpendicular width are usually around 4. However, the measurements typically refer to the highest point of some sail section, while aerial imagery shows that the sail width does not vary as much as the sail height but is rather constant. The results of (Lensu, 2003) indicate that the highest point of a sail section is typically 2.5 times the average sail height, and ~~102 respectively. Thus especially the highest class retains its delineation in this method change.~~

~~In the present study the BPN statistics is at focus however. For selected pair of L and BPP a certain finite, discrete distribution with maximum value L^2 becomes defined for~~ thus the average value of R random sail crossings is about 10. To add, the ~~BPN. A distribution model parameterised by L and BPP would provide basis for the study of interrelations between contextual images defined for different scales L. The principal approach towards the BPN statistics is to consider how the statistics is changed in BPP changes~~Rayleigh criterion counts as singular ridges certain wider multiple peaked formations. Deformed ice fields also include scattered rubble and other diffuse roughness not accounted for in the estimates. To include the contribution of these, the value $R = 13$ is adopted.

~~As an introduction to the theme, the BPN values are obtained from a non-overlapping $L = 8$ block tiling (i.e. not as a sliding operation of contextual images). The BPP for a 1024x1024 image is increased from 10% to 15%. For each block this induces a BPN increase from n to $n + m(n)$ where $m(n)$ is~~ The cutoff sail height affects both ridge density and ridge height. To estimate the cutoff effect, the extrapolation model by (Lensu, 2003) is applied. It is assumed that the average sail height is representative of the ~~number of added bright pixels. In Figure **??** the range of $n + m(n)$ is shown for each value n together with the distribution $m(n)$ given $n = 11$. The mean value of $m(n)$ increases first with n, but levels off in the mid-range and starts to decrease for higher BPN. For $n = 11$ and other selected the test values $m(n)$ follows Poisson distribution. Thus the change $m(n)$ can be modeled as resulting from a process where new bright pixels are assigned randomly to the blocks with a rate that depends on n. This observation leads to the generative model for the BPN distributions in the next section.~~ whole data set and only the variation of ridge density is at issue. For the present LIDAR profile data with a cutoff height of 0.4 m and an average sail height 0.65 m, the model provides estimates that the true average height is $h_a = 0.48$ m and that the true densities are 2.0 times the observed density.

~~The increase in BPN values for $L = 8$ blocks when BPP is increased from 10% to 15%. On the left, the range and mean value of increased BPN. On the right, distribution of BPN increase for blocks with 11 bright pixels.~~

3 ~~Statistical model~~

2.1 ~~Ridge sail rubble and ridge sail numbers~~

~~In the present approach the statistics of SAR images from ridged ice cover is described in terms of bright pixel numbers (BPN) in non-overlapping pixel blocks. High resolution (1.25 m) images resolving individual ridge sails are used in the development. Bright pixels are defined by an intensity threshold, or by equivalent bright pixel percentage (BPP), and the numbers of bright pixels in the pixel blocks are counted. The parameters of the approach are the block side length L in pixels and the BPP (equivalently, intensity threshold for the BPP). The guiding hypothesis is that BPN values increase on the average with the area covered by ridge sail rubble. It is less evident whether or not the BPN values increase with ridge height if the sail rubble coverage remains the same. Another issue is the interpretation of lower resolution SAR images not resolving individual ridges~~Taken together, the ridge rubble coverage RRC along a profile is:

$$\frac{RRC}{A} \approx \frac{\pi}{2} \times R \times h_a \times \lambda \tag{1}$$

$$\approx \frac{\pi}{2} \times 13 \times 0.00048 \times 2 \times lambda, \tag{2}$$

where all quantities are in kilometres (h_a=average height, λ=observed ridge density). A unit increase in the observed ridge density for 0.4 m cutoff data increases the along profile rubble coverage by 1.96%. However, as the interpolation factors are rough estimates, the value 2% is used instead.

~~Sail rubble can be quantified from two-dimensional topographic data but only few local datasets exist from the Baltic, one analysed data being (Similä et al., 2010). The more extensive validation data consists of airborne ice surface profiles from which ridge sails and their heights are identified. Profile data will retain its importance also in the future as narrow beam satellite laser altimetry by IceSAT−2 is likely to become a major source of validation data (Fredensborg Hansen et al., 2021). For pencil beam airborne laser data, which is used in this study, ridge sail statistics is described in terms of profile segments of length L. The numbers of ridge sails reaching above certain height threshold in the segments are counted (ridge sail numbers, RSN). Segment length L and~~ If the profiling flights have crossed an area multiple times in different directions, which for our data was the case for coastal ridge fields near the flight base, the estimate is representative of areal rubble coverage. For a singular crossing, the ~~sail height threshold are parameters. They are conceptually equivalent to the pixel block side length and the pixel intensity threshold for SAR images.~~ relationship involves randomness and is generally the more reliable the larger the considered area is, provided that homogeneity of ridging conditions persists. On the other hand, independent estimates of rubble coverage from SAR or other data can be converted to ridge density interpreted either as an average of multiple crossings or as the probability to find the said density in a singular random crossing.

~~Correlations are expected between RSN values and the sail rubble coverage in the horisontally extended area from which the linear profile data samples. In the Section 3.1 we will derive Equation 2, which yields an estimate that on the average one ridge per km corresponds approximately to 2% sail rubble coverage in km^2. Thus, as mediated by the sail rubble coverage, correlations between bright pixel numbers and ridge sail number is expected. Due to temporal separation and ice drift, BPN values in pixel blocks and RSN values in segments cannot usually be directly compared for matched pairs of blocks and segments. To this adds the fact that Eq. 2 holds as such only for extended homogenous ridge fields while the local RSN values are random linear samples from the local two-dimensional sail geometry. The approach therefore seeks to demonstrate that both BPN and RSN follow the same statistical model and to establish parametric relations between the two.~~

2.1 Threshold process

For an idealised SAR image with accurate real-valued intensities, the pixel values can be arranged into strictly increasing order. ~~The derivation of the statistical model for the BPN in pixel blocks is based on the following approach. In the idealised setting, starting from~~ Starting from an empty image matrix and from the brightest pixel, the pixels of the ordered series ~~are added one by one~~ can then be added to the matrix one by one. It can then be studied how the probability for the BPN to increase by one depends on the pixel block state <L,BPN,...> ~~of the block as defined by side length~~ by L, BPN, and possibly by other descriptors. ~~These increase~~ The probabilities can then be used to formulate recurrence relations ~~that can be used to generate~~ generating finite BPN distributions. ~~This is manageable at least when the relations depend linearly on BPN, which will be also the assumption behind the distribution models applied in the present approach.~~

For ~~integer valued SAR imagesthe process is realised by starting~~ integer-valued SAR images, the process starts from the BPN values for maximum intensity ~~, usually 255, and adding step by step~~ and proceeds in unit integer steps by adding pixels of subsequent lower intensity. This ~~means decreasing the intensity threshold by unit integer steps, and the process is designated here as~~ is designated as the threshold process. The ~~increase~~ increased probabilities are replaced by ~~increase~~ increased rates, that is, the relative number of events of unit BPN increase. For RSN, an analogical process decreases the sail height threshold ~~with~~ by small values, starting from a threshold equalling the highest ridge. The increase rates ~~are then intepreted as increase~~ of the threshold process are then interpreted as increased probabilities of an idealised process. ~~Strictly taken this requires that~~ This is legitimate if the number of increase events larger than unity is relatively small for each step. ~~In practice the steps are limited from below by the discreteness of the SAR intensity, or by the nominal reading accuracy of profiling instruments, typically 1 cm.~~

The threshold process is continued to ~~certain BPP~~ a certain pixel intensity or ridge sail height cutoff, called a target threshold~~above which the statistics is assumed to be dominated by ridges~~. The derivation of ~~statistical model from the increase rate~~ the statistical model is based on the following observation. The ~~target threshold being set, the SAR~~ intensity or ridge sail height values higher than or equal to the target threshold can be randomly permuted. This changes the increase rates, generating another threshold process. However, the ~~end result, or the~~ BPN or RSN distribution observed on the target threshold level ~~,~~ is the same for both processes. Thus, the new increase rates can be used to generate the observed distribution. The random permutation has the merit ~~that it removes~~ of removing the spatial correlations of intensities or sail heights ~~. The threshold~~

process reduces so that the threshold process is reduced to a random deposition processthat does not depend on intensities or sail heights.

2.2 Scale system of distributions

The threshold process and the distribution model are presented for ridge sail numbersRSN statistics. The case for bright pixel numbers BPN is conceptually analogical . However, the BPN statistics involves features present in SAR images but not in profile data: material sea ice characteristics such as mm-cm scale surface roughness of ice and inhomogeneities in the uppermost part of ice, but involves complications not present in RSN statistics: discreteness of integer data, resolution set by pixel size, and the limit L^2 as the maximum BPN value.

In RSN analysis, surface profile data is divided into segments, and the numbers n of sails in the segments are counted. Segment length L_i is a variable parameter. A discrete distribution $k(n_i)$ for sail number n_i becomes defined for each scale L_i. If $L_j < L_i$ is a shorter segment, a conditional distribution $k(n_j|n_i)$ becomes defined. This can be interpreted as the conditional probability to find n_j sails in an L_j-segment nested inside an L_i-segment containing n_i sails. The $k(n_j|n_i)$ can be also called downscaling probabilities as they can be used to derive distribution $k(n_j)$ from $k(n_i)$. This The approach can be extended to a cascade of scales, constituting a scale system of distributions. It is convenient if shorter scales divide longer scales, preferably as a binary cascade where segments are successively bisected.

In an idealised threshold processes ideal threshold process, the sail heights can be are arranged into strictly increasing order and added one by one to the segmented profile. Two nested segments with lengths $L_i > L_j$ are considered and the shorter segment L_j is divided further so that the longer segment L_i is divided into segments with length L_j and $L_i - L_j$. If the sail is added in the process to $L$$L_j$-segment, it has a certain probability to become of getting added to each subsegment. This probability must satisfy the additivity condition $P(L_i) = P(L_j) + P(L_i - L_j)$. In general the probabilities depend on local conditions, especially sail height correlations. If the correlations are removed by a random permutation of heights the The simplest assumption satisfying the additivity condition is $P(L_i \sim n_i + aL_i)$. This assumption condition is $P(L_i) \sim n_i + aL_i$, which leads to the hypergeometric distribution (Lensu, 2003):

$$k(n_j|n_i) = \frac{\binom{aL_j+n_j-1}{n_j}\binom{aL_i-aL_j-1+n_i-nj}{n_i-n_j}}{\binom{aL_i+n_i-1}{n_i}}, \quad n_j = 0, 1, \ldots, n_i. \tag{3}$$

If $L_i/L_j \gg 1$, then the finite and discrete distribution $k(n_j|n_i)$ is approximated by $k(n_j)$ and $k(n_j)$ is approximated by the negative binomial distribution

$$k(n_j) = \binom{aL_j + n_j - 1}{n_j} p^{aL_j}(1-p)^{n_j}, \quad \text{where} \quad p = \frac{aL_j}{aL_j + < n_j >}, \tag{4}$$

and further , and furthermore, if $< n_j >$ is large, the continuous approximation of Eq. 4 is the gamma distribution:

$$f(n_j) = \frac{1}{\Gamma(\alpha)}\beta^{\alpha} n^{\alpha-1} e^{\beta n_j betan_j}, \quad \alpha = aL_j, \quad \beta = \frac{aL_j}{< n_j >}. \tag{5}$$

It is convenient to assume that ~~L is~~ L_i is a regional scale where ~~the variation in ridging conditions is~~ ridging statistics are described by the negative binomial $k(n_i)$, as approximated by the gamma distribution. The hypergeometric $k(n_j|n_i)$ ~~can~~ is then be used to describe local variation.

The ~~scale system is validated along~~ statistical model is validated in two stages. ~~The~~ First, the additivity condition is ~~first~~ validated by conducting a threshold process for selected scales and target thresholds and observing whether the increase rates have a linear dependence on the ~~sail number. As the threshold process is an artificial device and process steps are incommensurate, the actual values of the linear parameters provide little information.~~ RSN or BPN. In the next stage, the distribution models are fitted to the data. In the sections to follow~~this is made by~~ , this is done by the observed mean and variance, and the goodness of fit is checked. The parameter a is obtained from the variance

$$var(n_j|n_i) = \frac{L_j n_i (aL_i + n_i)(L_i - L_j)}{L_i^2 (aL_i + 1)} \tag{6}$$

and

$$var(n_j) = \langle n_j \rangle + \frac{\langle n_i \rangle^2}{aL_j} \tag{7}$$

for the hypergeometric and negative binomial models, respectively. ~~We remark that the~~ The variance for the negative binomial distribution is larger than the mean, which ensures that a is positive in Eq. 7. The parameter a quantifies ~~in the threshold process the~~ the relative strength of the component process of the random spatial deposition of sails, that is, the Poisson process. If the validation results agree for test cases selected from a certain scale range, it can be concluded that the scale system is applicable over the scale range~~and for any combination of scales~~.

2.3 ~~Observed rates and distributions for ridge sail number~~Simulation of SAR texture by the threshold process

~~The profile data set described in Section ?? was used to study the scale system and its generative threshold process. All profile data consisting of~~ To analyse the BPN threshold process in full detail requires that bright pixels are added one by one in process steps. For integer-valued images, this cannot be attained. On the other hand, it is possible in a validation approach where the generative hypotheses are tested by simulating the generative process. The simulation commences from a certain stage of the observed threshold process. New bright pixels are added one by one following the assumed probabilities and possibly other conditions. The simulated result is then compared with the observed one.

A binary image with value 1 (white) for an observed low percentage of brightest pixels is used to seed the process. The simulation changes the value of black (zero) pixels into white, one at a time. This is done by a scale cascade, which is assumed here to follow the linear generative hypothesis. The first step divides the image into four rectangles along randomly chosen vertical and horizontal lines. To each rectangle is assigned weight $aN0 + N1$, where $N0$ is the number of pixels, $N1$ is the number of white pixels, and $a < 1$ is a parameter that controls the relative strength of a random spatial placement (Poisson process). One of the rectangles is selected for the next step with a probability defined as the ratio of rectangle weight to the sum of weights. The selected rectangle is divided further into four, and the cascade is continued until the rectangle contains only one black pixel that is changed to a white pixel. The process repeats until a preset number of white pixels is reached.

The simulation approach can also be applied to other generative hypotheses. Imposed maps of spatially distributed weights can be used to include spatial aspects of the generative process, like correlations, homogeneity, gradients and support, i.e. the subregion outside of which the process is not active.

3 Results

3.1 Observed threshold process rates and distributions for ridge sail number

From the profile data set described in Section 2.1, profiles exceeding 5 km in length ~~was~~ were selected and truncated to be divisible into 1.6 km, in total 2256 km. ~~In the determination of RSN values for variable segment lengths~~ For RSN analysis the segment length L the ~~binary~~ cascade [50,100,200,400,800] (meters) was used. The threshold process ~~was set to decrease~~ decreased in 0.01 m steps from 2.5 meters ~~, which value selects~~ (10 ~~ridge sails from the whole dataset. The weight of cases where RSN values increase by more than one in a step increases exponentially with the decreasing threshold. This affects the results significantly for thresholds smaller than 0.5 m. The~~ ridges). The target threshold was set ~~therefore~~ to 0.5 m ~~, selecting~~ (18638 ridges~~, and the number of threshold process steps was 201.~~).

The increase rates per step were determined as the mean value of RSN increases, including zero increase~~. The~~ , and the presented results are for the pooled data comprising all steps to the 0.5 m target threshold. ~~However, the results were essentially similar if a higher target threshold was used.~~ The increase rates were calculated both for the original data and for ~~the data with~~ randomly permuted sail heights. The results ~~are shown in Figure ?? where the graphs are truncated for the tail part of RSN values for which the few RSN increase instances show~~ shown in Fig. 5 disregarded the tail part with an excessive variation. In the right panel of ~~Figure ??~~ Fig. 5, the highest RSN ~~already corresponds~~ values correspond to ridge density 160/km, a value characteristic ~~to rubble fields~~ of rubble fields with no level ice visible. The increase rates were ~~generally linear for the randomly permuted data. There is~~ linear with a slight superlinear bend~~when both L and RSN have higher values~~.

The ~~increase rates for the original, non randomised data are shown also in Figure ?? for $L = 100$ and are seen to~~ rates for non-randomised data deviate after beginning from linear to sublinear increase. For other scales, the behaviour was similar, and for long L, the rate more or less settled to a constant value in its tail part. ~~Sail height correlations are the likely reason for these observations. These~~ A likely reason is that sail height correlations that arise naturally as ~~the thickness of parent ice from which the ridges are created varies spatially and~~ block thickness (a parameter controlling ridge sail height) vary spatially during the course of the ice season. ~~Clear correlations were also~~ Correlations were indeed found between RSN and the average sail height~~for a segment~~.

~~Sail number increase rate for in a threshold process with target threshold 0.5 m. Left: Rate for observed sail heights and randomised sail heights for segment length $L = 100$ m . Right: Rates for randomised sail heights for different segment lengths.~~

The hypergeometric and negative binomial distributions were fitted to the data with observed ~~parameters (~~mean and variance~~)~~. The negative binomial $k(n_i)$ agrees well with the empirical distributions derived from the full dataset in ~~Figure ??.~~ Fig. 6. Only the number of empty segments is overestimated for 200 m and 400 m segment lengths. ~~Figure ??~~ Fig. 7 shows the hypergeometric distributions $k(n_j|n_i)$ for the conditioning scale $L_i = 1600$ m and for the range [50,100,200,400] of the

subsegment scale L_j. ~~Results~~ The results for two values of conditioning RSN, $n_i = 16$ and $n_i = 72$, are shown. These are equivalent to ridge densities 10/km and 45/km for the segments L_i. The agreement is good, considering that the subset size is limited by fixed value n_i. Similar results are found for other combinations of L_i, L_j, and n_i. The hypergeometric model was derived from the assumption that the rate of the RSN increase for the segment length is proportional to $n + aL$.

The parameter a is obtained from the mean and variance and is generally found to decrease with L following ~~a~~ the power law. For the ~~shown hypergeometric case~~ hypergeometric case shown, the exponent has about the same value of 0.5 for all values of the conditioning n_i ~~ranging~~ from 16 to 72. The parameter a ~~can be interpreted as~~ was interpreted as the relative Poisson intensity~~that~~ , which also provides the rate of sail appearances to empty segments in the threshold process. ~~The threshold process is basically governed by the physical presence of ridge rubble in the profile segments. In an idealised setting, if there is not rubble present it cannot be detected by the threshold process either~~If there is no rubble present in the segment, it can be said to consist of level ice and cannot experience a change of RSN from 0 to 1, either. The Poisson parameter of level ice segments is zero, and the observed Poisson parameter a is obtained by multiplying the true Poisson parameter of rubble segments by their relative coverage. Thus the power law suggests that the area covered by ridge rubble has fractal geometry. ~~This point is addressed further in the Discussion section.~~

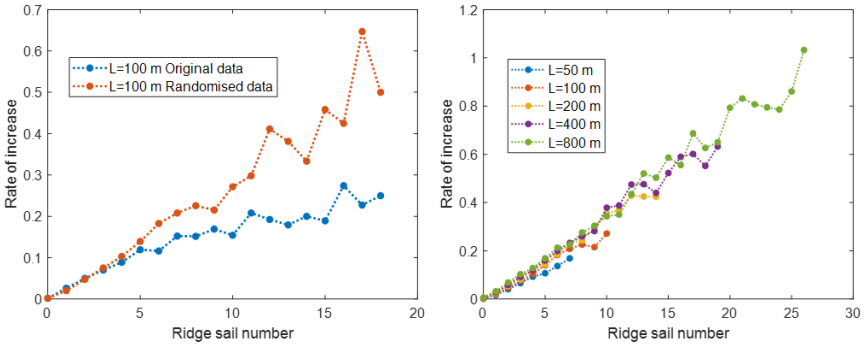

Figure 5. Sail number increase rate for in a threshold process with target threshold 0.5 m. Left: Rate for observed sail heights and randomised sail heights for segment length $L = 100$ m . Right: Rates for randomised sail heights for different segment lengths.

3.2 ~~Observed rates and distributions for BPN~~Characteristics of high-resolution SAR

~~For the BPN threshold process analyses the high resolution~~ The pixel size of the March 2016 Stripmap image is 1.25 m, which resolves backscattering signatures from individual ridges. The size of the image (Fig. 3)is 19x19 km, but for analysis and visualisation, different subimages were also used, principally 7000x7000 (8.7x8.7 km) and 1024x1024 subimages with representative ridging signatures. To proceed following the approach outlined in Section 2.1, a certain bright pixel percentage (BPP) is selected and a binary image with unit values for the bright pixels is generated. The variation of bright pixel density is described in terms of bright pixel numbers (BPN) in pixel blocks with variable side length L.

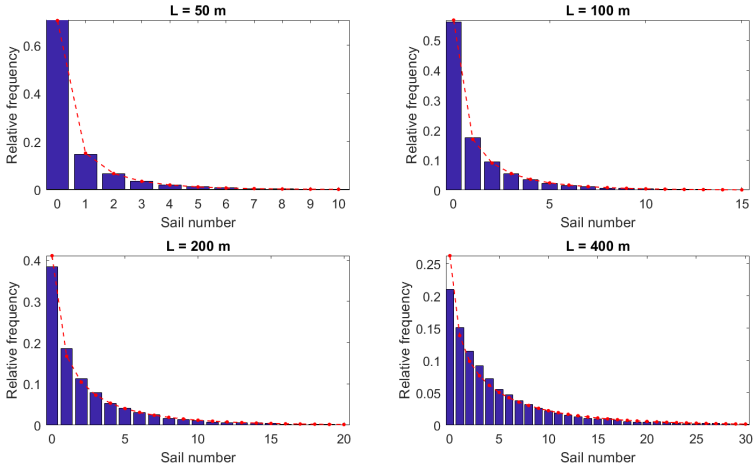

Figure 6. Negative binomial fits to the RSN distribution for the full dataset and for different segment lengths.

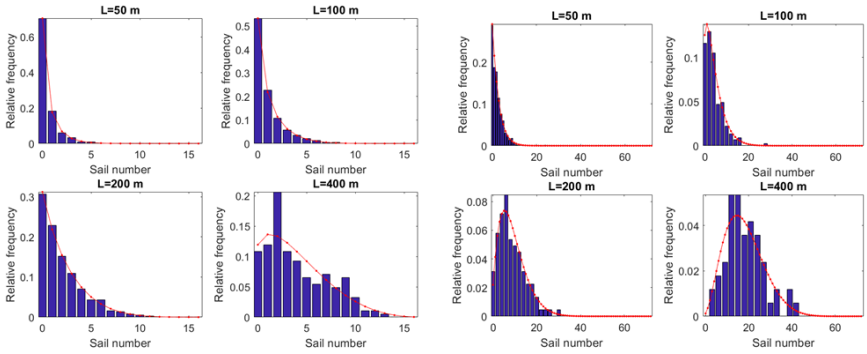

Figure 7. Hypergeometric fits for distributions $k(n_j|n_i)$ conditioned by $L_i = 1600$ m and $n_i = 16$ (left panel group) and $n_i = 72$ (right panel group). The scales L_i belong to [50,100,200,400].

Two derivative image types are also presented. Following the BPN approach, the first derivative replaces (as a sliding operation) pixel values with BPN values calculated for pixel blocks centred at the target pixel. This is accomplished by a convolution with a LxL all-ones kernel. The result is termed 'contextual image', as the visibility of ridging signatures and their effective resolution depend on BPP and block side length L, which can be chosen to suit the application context. The other derivative is 'category image', which divides the brightest 30% of pixels into three 10% classes, either for the original or the contextual image.

In the category-image version of the Stripmap image, fig. 3, ridging features appear to be visually delineated by the brightest 20

These observations agree with the results by (Manninen, 1992) and (Carlström and Ulander, 1995) that indicate that bright returns from ridge rubble depend on random factors like a favourable orientation of blocks, while the returns from the remaining sail may fail to be clearly distinct from the surrounding level ice. The apparent randomness also corroborates the assumption that the density of the bright pixels in the image is proportional to the coverage of ridge rubble.

In the contextual image and its category image rendering, Fig. 17, the sliding block side length is $L = 101$ (126 m), and the BPP is chosen to be 20% or comprising the red and yellow pixels of Fig. 17. It is seen that the ridging signatures are enhanced and their connectedness improved in the contextual images (Fig. 17).

3.3 Observed threshold process rates and distributions for high-resolution BPN

For the analyses of 7000×7000~~subimage was used. Instead of contextual image generated by a convolution operation, the image was~~ , the upper left corner subimage of the Stripmap image was used in order to avoid the refrozen lead visible in Fig. 3. The image was divided into non-overlapping pixel blocks with ~~varying~~ side length L, measured in pixels. The intensity threshold was decreased by unit integer steps, starting from 255, and the rate of BPN increase as a function of BPN was obtained for each step. In the presented results, the rate data comprises all steps down to the target threshold. In the subimage, 1.2% of the highest intensities are saturated to 255. This percentage is equal to that for the intensity band [218,254] and would correspond to the extending of the exponential tail of the intensity histogram beyond 255 to 350. This somewhat affects the results for the initial steps of the ~~threshold cascade~~process.

Analogically to the RSN analysis, the pixel intensities above and including the target threshold were randomly permuted. ~~The increase rate was investigated first for a fixed block side length L and varying target thresholds expressed as BPP. Then the same was done for varying~~ In Fig. 8, the block side length ~~and for a fixed target threshold. The first test case is presented for $L = 36$ in Figure **??**,where the~~ is set to $L = 36$ and the target intensity threshold values [182,149,118,86] are chosen, corresponding to BPP values [5,10,20,40]~~correspond to intensity thresholds 182,149,118,86. Similarly as~~ . As for the RSN~~the absolute~~ , the magnitude of the rates is not relevant, ~~only their possible linearity. For presentation purposes the rates~~ and they have been scaled so that the sum rate equals L^2 or 1024. The different degrees of saturation then separate the point clouds in ~~Figure **??**. Linear dependence of rates on BPN~~ Fig. 8. Linearity is observed unless the saturation of the pixel block is felt ~~. This occurs~~ after 3/4 of the block capacity is filled~~and affects significantly only cases BPP 20% and 40%~~.

~~The~~ In the other test case ~~is presented for BPP 80% in Figure **??**, where~~ in Fig. 9, the BPP is set to 20% (target intensity threshold 118), and the block side length increases ~~in binary fashion~~ from 4 to 128. In ~~addtion to the~~ addition to the same scaling of rates ~~described above the~~ as in the first test case, the BPN range $[0, L^2]$ has been scaled to [0,1]. The results are similar ~~as above~~to the first test case. For comparison, the same result is shown for the original data where the pixel intensities are not randomised. For higher L, the relationship is then approximately linear for small relative BPN values, but otherwise, it is quadratic~~and the second order fit is also symmetric within the range of nonzero rates. The quadratic behavior is discernible also in Figure **??**.~~ Intensity correlations are the ~~apparent reason~~likely reason, but no further conclusions are attempted. ~~Also for the variable BPP case the nonpermuted rates have quadratic dependence on BPN although the data grows diffuse for higher~~

~~BPN if BPP is other than 40%. The rate data 90% percentiles for BPP= $[5, 10, 20, 40]$ are BPN=$[134, 240, 403, 637]$. Linearity is not a very good approximation for the 90% range, and is less good for higher BPP.~~

~~The BPN increase rates for pixel block side length 36 and BPP increasing from 5% to 40% in binary fashion.~~

~~The BPN increas rates for BPP 20% and for pixel block side length increasing from 4 to 128 in binary fashion.~~

The agreement of the proposed distribution system with the data is again good. ~~Empirical distributions~~ Distributions were calculated from block tiling of the 9216×9216 (11.5×11.5 km) upper left corner subimage. ~~Figure ??~~ Fig. 10 shows negative binomial distributions $k(n)$ fitted by observed mean and variance ~~. BPP is~~ for BPP 10%~~and the results for~~ , and three scales are shown. The fourth subplot shows the model parameter a as obtained from the mean and variance for the binary cascade of scales $L = 8, 16, \ldots, 256$ ~~,~~ and for three BPP values. The power law exponents ~~varies~~ vary from -0.37 to ~~-0.45~~ 0.45 and are thus close to but somewhat smaller than the values obtained in the RSN analysis. Also, the negative hypergeometric model $k(n_j|n_i)$ conditioned by scale L_i and BPN value n_i applies well. ~~Figure ?? show~~ Fig. 10 shows the results for selected combinations of Li, Lj and n_i. The conditioning scale cannot ~~exceed much~~ much exceed the value $L_i = 16$ as the number of instances n_j for conditioning pairs (L_i, n_i) ~~decrease~~ decreases as L^{-4}.

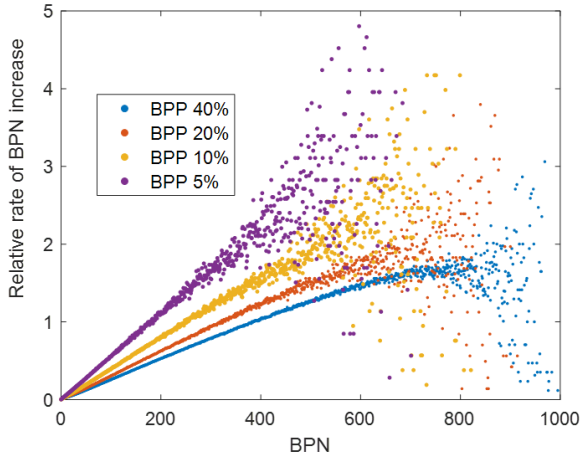

Figure 8. The BPN increase rates for pixel block side length 36 and BPP increasing from 5% to 40% in binary fashion.

3.4 ~~Simulation of~~ Simulated high-resolution SAR texture ~~by the threshold process~~

The ~~hypergeometric distribution model was derived from the assumption that the RSN/BPN increase rate of the threshold process has linear dependence on RSN or BPN. This assumption was validated by the rates calculated from data and by fitting the model to data by mean and variance. To analyse the increase probabilities of the threshold process in fullest detail would require that ridge sails or bright pixels are added one by one by process steps.For present integer valued images this cannot be attained. On the other hand, it is possible to test generative hypotheses by simulating the corresponding generative process.~~

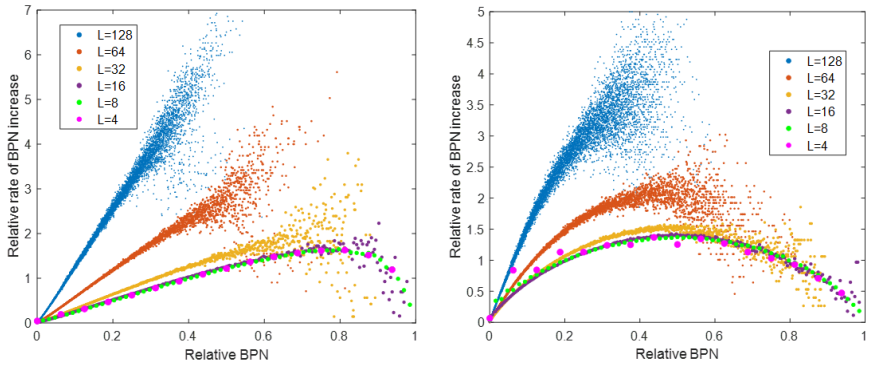

Figure 9. The BPN increase rates for BPP 20% and the pixel block side length increasing from 4 to 128 in binary fashion.

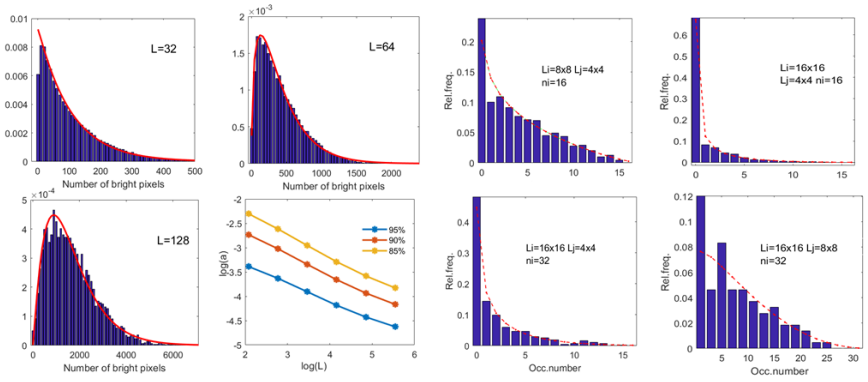

Figure 10. In the left panels BPN distributions and their negative binomial fits for BPP 10% and three different pixel block side lengths L. The parameter a is also shown for a scale cascade $8, 16, \ldots, 256$ and for three different BPP. In the right panel hypergeometric fits for conditional BPN distributions for different combinations of conditioning scale L_i and conditioning BPN n_i.

~~The simulation commences from a certain stage of the observed threshold process. New objects, here bright pixels or sails, are added one by one following the assumed transition probabilities. The simulated process is then compared with the observed one. This allows also the analysis of the spatial aspects of the generative process, most importantly homogeneity and support, or the subregion outside which the process is not active.~~

~~This approach is formulated here for SAR images using the linear assumption but including certain additional restrictions related to the spatial distribution. A binary image with value 1 for low percentage of brightest pixels is used to seed the process~~simulation algorithm was applied to the 1024x1024 subimage indicated in Fig. 3. The white pixels of the initial binary image correspond to BPP 3%. The simulation ~~changes the value of zero pixels into one, one at a time. This is done by a scale cascade following the linear generative hypothesis. The first step divides the image into four rectangles along randomly chosen~~

~~vertical and horizontal lines. To each rectangle is assigned weight $aN0 + N1$, where $N0$ is number of pixels, $N1$ number of occupied pixels, and $a < 1$ is a parameter that controls the relative strength of random spatial placement (Poisson process). One of the rectangles is selected for next step with a probability defined as the ratio of rectangle weight to the sum of weights. The selected rectangle is divided further into four and the cascade is continued until there is only one non-occupied pixel in the rectangle. The status of this pixel is changed to one and the process repeats until a preset number of nonzero pixels is reached.~~

added 10% so that the resulting BPP is 13%. If $aN0 \gg N1$, the Poisson process dominates the simulation step, but overall ~~the process inevitably~~ , the process gravitates towards image areas with a higher density of ~~nonzero~~ white pixels. However, if the fraction of ~~nonzero~~ white pixels is initially low, the Poisson component process tends to add nonzero pixels into larger empty areas, ~~creating first~~ first creating dispersion and then spurious clusters. To reduce this, an additional condition requires that ~~the nonzero~~ in a process step, a white pixel cannot be added within a rectangle if its fraction of nonzero pixels is below a threshold Co and the rectangle size is within certain limits $[N1, N2]$. This effectively means restricting the support of the process.

The ~~simulation process was applied to the same 1024x1024 image as in Figure ??. The initial binary image corresponds to BPP 3% . The simulation added 10% so that the end result BPP is 13%. The~~ parameters were $a = 1/20$, $Co = 1/100$ ~~,~~ and $[N1, N2] = [100, 20000]$, and the results are shown in ~~Figure ??~~ Fig. 11. Although not matching exactly on ~~pixel level~~ the pixel level, both 13% images exhibit the same pixel density variations. ~~Convolving with 21×21 kernel the and generating~~ For contextual and category images ~~similar to those shown in Figure ??~~ for $L = 21$, the results for the real and simulated 13% images match almost exactly, that is, they contain the same information at scale $L = 21$. The results provide additional corroboration for the soundness of the generative hypothesis. They ~~provide also~~ also provide the insight that certain parts of ~~'non deformed'~~ 'non-deformed' ice should be left outside the ridging statistics, a feature ~~suggested also previously~~ also previously suggested by the emergence of power law exponents for the parameter a in the distribution fits. The parameters of this demonstration were determined by simple experimentation, but more systematic approaches can be conceived. Especially, ~~the~~ intensity values could be incorporated, which would introduce spatial intensity correlations, and the fractality suggested by the distribution analysis could be encoded into the simulation steps.

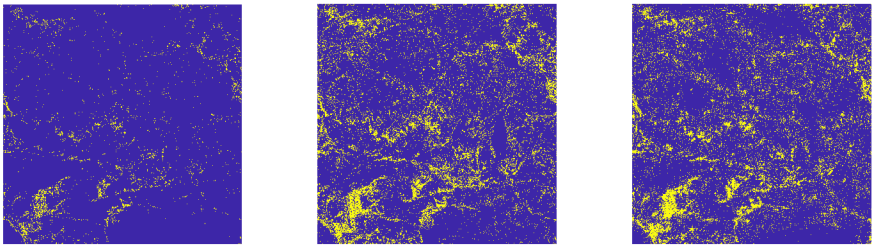

Figure 11. BPP 3% binary image, BPP 13% image, and the BPP 13% image generated from the BPP3% image by the simulation algorithm.

4 ~~Data analysis for medium resolution SAR data~~

3.1 SAR and ~~LASER~~ LIDAR comparison for the 2011 image

~~To analyse~~ The analysis of ridged areas in the ~~TSX ScanSAR image of resolution~~ 20 m ~~we proceed~~ resolution TSX ScanSAR image proceeds in a similar manner ~~than in~~ as the analysis of ~~high resolution SAR dataabove. As is validated extensively the highest backscatter values in the Baltic Sea are mostly generated by the deformed areas,e.g., (Mäkynen and Hallikainen, 2004) . The following deformation types were included: ridges, rubble fields and ice channels filled with rubble and brash ice. The ridges as well as the ice channels appear in the SAR image as bright filaments if the SAR resolution is fine enough.~~

~~The test area covered by the TSX SAR imagery with resolution of 20 m.~~

~~The tools in the analysis are a pixel block and the intensity values above a preset threshold as in the high resolution case. We examine the~~ high-resolution SAR data. The basic SAR tools are the bright pixel percentage (BPP) and the counting of bright pixel numbers (BPN) in pixel blocks. The target is distributions $f(x)$~~distribution where the argument~~ , where x ~~has the value of the deformed areas inside pixel block which are abbreviated here as RRC (ridge and rubble coverage) and its unit is percentage. The resolution of 20 m in the TSX image is sufficient to detect part of the ridges, see **??**. For the navigational purposes the rubble filled ice channels form an obstacle for the winter shipping as discussed earlier. Hence the ice channels are not treated separately from other forms of ice deformation~~is the estimated ridge rubble coverage (RRC) in pixel blocks (SAR RRC) or their ground truth counterparts as determined from LIDAR surface profiling flights (LIDAR RRC).

~~We note that the terms BPN and RSN which were essential for the statistical treatment of the high resolution SAR datain Sections **??** and **??** are equivalent to the terms SAR RRC and HEM RRC utilised in this Section. Already in the analysis of high resolution SAR image the equivalency of the terms was stated.Our focus in this Sectionis on the relationship of the areal coverage between two different datasets. Hence we prefer the terms SAR and HEM RRC.~~ The essential assumptions are that LIDAR RRC can be estimated from profile data, Section 2.2, that the bright pixel number can be used as a proxy for SAR RRC and also for 20 m resolution data, and that both RRC concepts inherit their statistics from the model for RSN and high-resolution SAR BPN, sections **??** and 3.3. It is noted that the 20 m resolution can still detect much of the ridging signature in Fig. 12 and that the simulation method described in Section 2.3 works.

The ~~first step in the analysis is to extract the bright pixel set with the~~ BPP is set to 20%~~threshold (here -14.4 dB) from the SAR imagery covering the study area. The set is denoted here with B. A binary image is constructed in which pixel has value one if it is in B and zero otherwise. The resulting image is called the seed image, see Figure **??**. Similarly to the results of Sect. **??** the specification of the threshold for B is not highly sensitive for our purposes, a topic we will discuss later. The ridging in the 20 m SAR data still preserves many of the properties of the very high resolution SAR imagery. One of these properties is that the in Sect. 2.3 introduced simulation method works also for the medium resolution image~~.

~~The seed image of 80% BPP derived from the TSX SAR imagery with resolution of 20 m on 28 February 2011 image .~~

~~The contextual image obtained from the seed image by convolving it with kernel of 15×15 pixels.~~

~~In the seed image the bright pixels in the set B~~ The exact BPP value is not essential, but the chosen one is expected to comprise most of the ridging signatures and not too much level ice. Similarly, as for the high-resolution image, the bright pixels

are mostly not connected to ~~each other. To increase the connectedness among the bright pixels and hence forming anticipated ridge structures, we convolve the seed image with kernel of 15 by 15 pixels to form~~ continuous ridging features. A convolution operation is then conducted, generating a contextual image ~~. The amount of pixels belonging to B in the convolution window is converted to percentage point and assigned to the center pixel of the convolution window in the contextual image. The maximum distance to a seed image pixel (20 m by20 m) which contributes to the computation of the center pixelvalue is always less than 170 m, mostly less than 100 m. The pixel size of the resulting contextual image remains the same~~ Fig. 12, where each pixel value of the original image is replaced by the number of bright pixels (BPN) in a 15 by 15 pixel block centred at the pixel. As the target is rubble coverage, the BPN values are changed to percentage points. The convolution operation acts similarly as in the ~~original SAR image (20 m).~~

~~The contextual image Fig. **??** reveals effectively~~ high-resolution SAR and effectively reveals the ridged areas ~~. The spatial arrangement of bright pixels in the seed image is such that the applied convolution operation~~ and connects many of the ~~ridge and the ice channel structures which one can detect visually~~ ridging structures that are only vaguely discernible in the original SAR imagery. ~~The magnitude of the backscattering generated by ridging in a pixel is roughly proportional to the size of rubble area covered by the pixel although subject to the random variation due to the arrangement of ice blocks (Manninen, 1992; Carlström and Ulander, 1995). Due to the curvilinear structure of a ridge and the variation of its ice block accumulations with respect to orientation and coverage the backscattering magnitude fluctuates in the neighboring pixels across which the ridge meanders. The convolution operation collects these only partially visible ridge pixels surprisingly well together. The convolution acts in the medium resolution SAR imagery similarly as in the high resolution imagery.~~

~~To derive ridging statistics the resolution~~

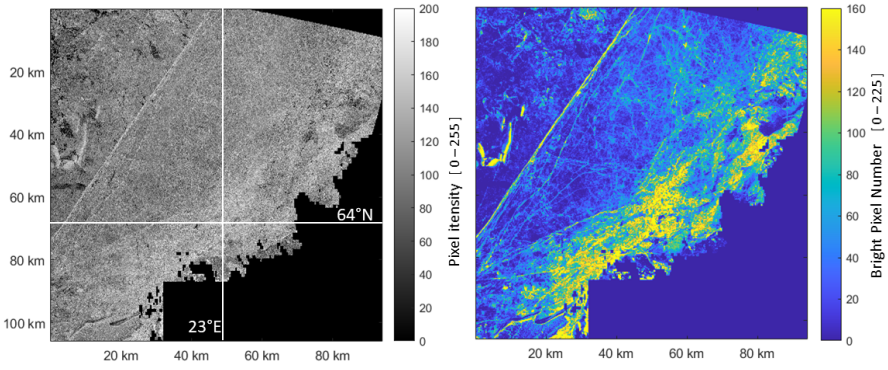

Figure 12. The test area covered by the TSX SAR imagery with resolution of 20 m. On the right is the contextual image with BPP 80%.

For comparisons between the SAR RRC and LIDAR RRC, the resolution of the contextual image is weakened to 1 km^2. ~~In the coarser resolution image each pixel comprises 50x50 contextual image pixels. The larger scale image~~ This coarser scale image Fig. **??** is called an analysis image~~. The pixel value in the analysis image~~ , and its pixel value is the mean of all ~~the~~

~~contextual image~~ pixels inside the ~~1 km^2 resolution pixel and is given in percentage points~~corresponding contextual image pixel block. These pixels ~~are~~ represent the SAR RRC ~~(SAR based ridge and rubble coverage) pixels.~~

~~The ridge rubble coverage can be estimated also from the profiling data (HEM RRC). In the computation of HEM RRC ridge density is multiplied by average ridge width which is obtained from average sail height by approximation. To provide realistic estimates the effect of cutoff sail height used in the profile analysis must be assessed, as well as the applicability of results reported on sail $width/height$ ratio which is noted $R = w/h$. Considering first the ridge width, the effect of oblique angles of sail crossings must be taken into account. If the ridges are randomly oriented, the average width is $\pi/2$ times the perpendicular width (Mock, 1972). This can also be interpreted that the ridge sail length per unit area $A = \text{km}^2$~~ and are compared with LIDAR RRC values determined in grid cells matching the pixels with respect to size and location. The LIDAR data were assigned to the grid cells in Fig. **??** using the coordinates included in the data. If the LIDAR grid cell contains data, its value is ~~$\pi/2$ times the ridge density. The reported R ratios are usually around 4. However, the measurements typically refer to the highest point of some sail section while aerial imagery shows that the sail width does not vary as much as the sail height but is rather constant. The results of (Lensu, 2003) indicate that the highest point of a sail section is typically 2.5 times the average sail height. This is the expected value sampled from the profiling measurements for which the value of R is then 10. To add, Rayleigh criterion counts as singular ridges a certain number of wider multiply peaked formations. Deformed ice fields usually also include scattered rubble and other diffuse roughness not accounted for in the extrapolation model. To include the contribution of these we increase the average width by further 30%. Thus the value $R = 13$ is used.~~

~~The cutoff sail height affects both ridge density and ridge height. If the cutoff is raised, ridge density decreases but average sail height increases. To estimate the cutoff effect the extrapolation model by (Lensu, 2003) is applied. It is assumed that the average sail height is representative for the whole data set and only the variation of ridge density is at issue.For the present laser profile data with cutoff height 0.4 m and average sail height 0.65 m the model provides estimates that the true average height is $h_a = 0.48$ m and that true densities are 2.0 times observed density.~~

~~Taken together, a unit increase in the observed ridge density for 0.4 m cutoff dataincreases the along profile rubble coverage by 1.96%:~~

$$\frac{RRC}{A} \equiv \frac{\pi}{2} \times R \times h_a \times \lambda$$
$$\equiv \frac{\pi}{2} \times 13 \times 0.00048 \times 2,$$

~~where all quantities are in kilometers (h_a=average height, λ=ridge density).~~

~~As deformed ice fields usually include scattered rubble and other diffuse roughness not accounted for the by the extrapolation model and when we also take into account the uncertainties involved, the value of HEM RRC is rounded to 2% of the pixel area for a single ridge~~ the ridge density detected in it, and the RRC in ~~Eq. 2. If the profiling flights have crossed an area multiple times in different directions, which was the case for coastal ridge fields near the flight base, the estimate is representative of areal rubble coverage. For a singular crossing the relationship involves randomness and is generally the more reliable the larger the considered area is, provided that homogeneity of ridging conditions persists.~~

Hence one ridge has about 2% RRC per km^2 and ridging with ridge density of 10 ridges/km occupy about 20% of the 1 km^2 unit area. We use this estimate for HEM RRC in the statistical analysis. Because one ridge in an analysis pixel corresponds to 2% rubble coverage, RRC can be directly converted to the amount of ridges, i.e. RSN, if needed. In the case of SAR RRC a direct conversion to BPN is not possible anymore in the analysis image.

The analysis image over the test area presented as a SAR RRC image. The units are percentage points.

The HEM flights over the test area presented as a HEM RRC image. The units are percentage points.

3.2 Combining SAR and Laser datasets

To each ridge the following quantities are attached: latitude and longitude coordinates as well as spacing (distance to previous ridge). From the profile data is already removed the ridges with sail height less than 0.4 m. The information of the spacing is not used in the computations.

A grid with 1 km^2 cell area for the profile measurements was formed. The coordinates of each grid cell corresponded to the analysis image pixel with the same resolution. Then we identified the profile measurements belonging to different cells. The value of HEM grid cell is the number of ridges detected in it (RSN). RRC for each grid cell is estimated as discussed above: multiplying the count of ridges percentage points is estimated by multiplying the density by 2%. All the grid cells with amount of 50 ridges or more were indicated to , Eq. 5. Ridge densities larger or equal than 50 then have 100% RRCbased on the ridged area estimates. About . This was the case for about 2% of all the cells where one or more ridges occurred had 100% RRC coverage. These cells situated near coast with nonzero ridge density and occurred only in the rubble field zone . It is possible that some of the ridges in these 100% RRC cells were measured more than once because these cells were in the area where majority of the HEM flights began, see Fig. **??**. close to the eastern coast.

As was pointed out in Section **??** 2.1, ice drift and additional deformation after the acquirement deformation occurred during the profiling campaign week after the acquisition of the SAR imageare present in the profile data but do not show up in the SAR imagery. Hence the comparison based on the one-to-one pixel correspondence is not adequate. We performed the comparison regionally between the two data sets. The sparsity of the HEM flights in many parts of the SAR image (Fig. **??**) reduced the amount of the HEM RRC grid cells. All nonempty profile grid cells in the SAR covered area were utilised when the regional distribution of RRC based on the HEM data was computed (As the ice drift could have been well over 10 km during the time gap, and the flights are from several days, it is not possible to establish a one-to-one correspondence between the RRC estimates for the SAR analysis pixel LIDAR grid cells, and the comparison was made regionally. All LIDAR data in the area covered by the SAR image was used for the RRC values in the LIDAR grid. Fig. **??**13(right). The SAR based analysis image is shown in RRC analysis image Fig. **??**. It covered all the profile measurement profiles and also areas between the HEM flight lines. The extent 13(left) includes all pixels outside the mask (N=7549 pixels). LIDAR data (N=1017 cells) comprise about 13% of the SAR image is larger than the HEM flight routes require. This is due to practical considerations. We wanted to preserve the structure of the SAR imagery. In addition ice drift made it impossible to determine corresponding points in the SAR and HEM data with any reasonable accuracy. The ice drift of R/V Aranda varied from 0.1 to 0.4 knots. The time difference between SAR

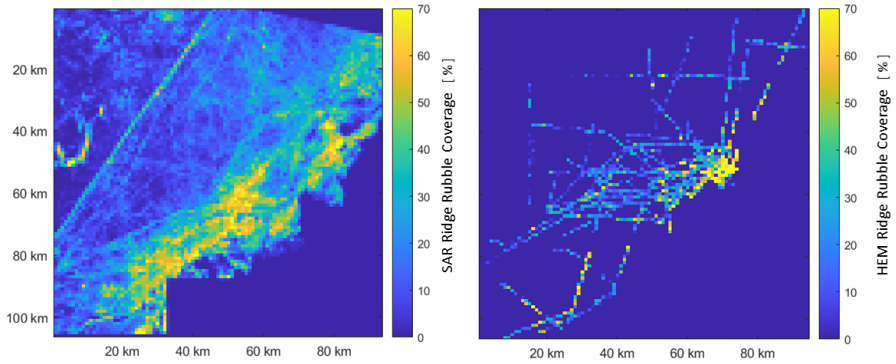

Figure 13. The analysis image over the test area presented as a SAR RRC image on the right and the corresponding LIDAR RRC image. The units are percentage points in both images.

~~and HEM data ranged from two to four days. Hence the trajectory length of ice drift could be well over 10 km during the time gap. The main ice drift direction was eastward.~~ pixels.

3.1.1 ~~The results~~

~~In this Section we compare the data sets based on the SAR imagery and the profile data. The samples from the both data sets have the same resolution. We consider their similarity using the~~ The two datasets are compared in terms of a quantile-quantile (Q-Q) plot for the ~~distributions. The use of Q–Q plots to compare two sample sets of data~~ respective distributions. This can be viewed as a nonparametric approach to comparing their underlying distributions.

~~Since the Q–Q plot compares distributions, there is no need for the values to be observed as pairs, as in scatter plot, or that the number of samples in the two groups being compared to be of same order of magnitude. There are about seven times more samples from the SAR RRC estimates (N=7549) than from the HEM RRC estimates (N=1017). The distinctive and most important feature in the Q-Q plot (Fig. ??) is that the~~ There is also no need to compare the grid values pairwise or have equally sized datasets. The quantile pairs are largely located along a line ~~. This implies that the distributions are linearly related which in turn implies that the~~ with a ratio of 1.34 between the quantiles (Fig. 14, the left panel). This indicates that the shapes of the distributions are similar ~~. Because the HEM RRC follows~~ and that they may belong to the same distribution family. As LIDAR RRC is expected to follow a gamma distribution (Eq. 5~~.), then also SAR RCC can be approximated by gamma distribution. This linear relationship was not anymore valid for the upper tail of deformation estimates, approximately for SAR RRC over 50 % and for HEM RRC over 75 % RRC. This can be expected because the SAR RRC values over 50% are in the data relatively rare. The relationship is also affected by the limited amount of the HEM flight lines.~~

~~The quantile-quantile plot for the SAR and HEM data sets.~~

~~From the general trend of the~~), this is then also expected for SAR RCC. For two gamma distributions, the linearity of the Q-Q plot entails that the shape parameters are equal, which also holds for the model Eq. 5 if the scale L_j and the process parameter

a are the same for both. The slope of the Q-Q plot ~~we can see that the ratio between the HEM/SAR quantiles remained almost constant, here about~~ then equals the ratio of the scale parameters, suggesting that a value of 1.34 ~~on the interval from 0 to 75% for the HEM data. As a consequence the distributions $f(a*x) = g(x)$ are~~ can be used as a scaling coefficient.

It was examined how close to each other ~~, where f is the underlying density of SAR RRC estimates, a is a weight coefficient (1.34) and g is~~ the ~~corresponding density for the HEM RRC estimates. The $1/a$ value is the slope of the line fitted to the quantiles in the HEM-SAR Q-Q plot. In the SAR-HEM Q-Q plot the slope is a.~~

~~We examined how~~ distributions of the SAR and LIDAR RRC are with and without the scaling coefficient of 1.34, Fig. 14. The original SAR and LIDAR RRC densities show the same basic shape but do not match well. When SAR RRC is scaled by 1.34, the match is improved, and the obtained mean values are very close to each other: 26.2% for the scaled SAR RRC and 25.9% for the LIDAR RRC. Converting the mean values to the number of ridges yields about 13 ridges per km^2 for both data sets. Gamma distributions were also fitted to both data sets. The maximum likelihood estimates for the shape parameter of the scaled SAR RRC gamma density is 1.7 and the scale parameter 15.5. The respective values for LIDAR data are 1.4 and 18.2. Thus, although the parameters of the fits are close to each other~~the distributions of the SAR and HEM RRC are with and without weight coefficient 1.34. The estimated densities for the analysis image RRC and the HEM RRC without weight coefficient are overlaid in Fig. **??**(left panel). The original SAR and HEM RRC densities show the same basic shape. The distributions illustrate that~~ , they are not equal.

The problems with the fit and agreement with gamma distribution mostly concern the tail part of the distribution. The linearity of the Q-Q plot was no longer valid for SAR RRC over 50 % and for LIDAR RRC over 75 % RRC. The SAR RRC values over 50% are relatively rare in the data, and highly ridged areas form proportionally a much larger fraction in the ~~HEM datathan~~ LIDAR data. Especially the rubble field hump seen by the end of the LIDAR distribution is not present in the SAR ~~analysis image data. This is due to the profile measurement arrangement where the HEM~~ distribution. As the LIDAR flights frequently flew over the large coastal ~~rubber field zone ,~~ rubble field zone (see Fig. **??**. ~~Consequently a significantly~~ 13), a larger proportion of the ~~HEM~~ LIDAR data was collected from this area than was the case with the SAR RRC data. The ~~difference explains also the breakdown of the linear relationship in the upper tail of the Q-Q plot (Fig. **??**). One can speculate that if the HEM flights were located more uniformly~~ scaling coefficient was found to increase with the area of SAR included in the comparison and varied from 1.3 to 1.6. With a spatially more uniform coverage of the LIDAR flights over the SAR image, the ~~weight coefficient would be closer to 1.~~ agreement would probably have been better for the tail part.

~~The SAR RRC density with weight coefficient 1.34 is compared to the HEM density in Fig. **??**(the rigt panel). We observe a high agreement in the distributions. The value of the weight coefficient changes if the area of the SAR image is extended. For the SAR-HEM comparison the weight coefficient varied from 1.3 to 1.6 depending on how the SAR image area of interest was defined. When the new weight coefficients were applied the SAR RRC distributions were quite similar to the one shown in~~ As expected, decreasing the BPP value increases the scaling coefficient when the SAR image extent and the LIDAR data stay fixed. Three cases were examined: For BPP 10 %, the scaling is 2.22, for 15 %, it is 1.61 and in the above analysis with BPP 20 %, it is 1.34. In all three cases, the QQ plot linear for its main part and the mean of the scaled SAR RRC distribution are always close to the LIDAR RRC mean.

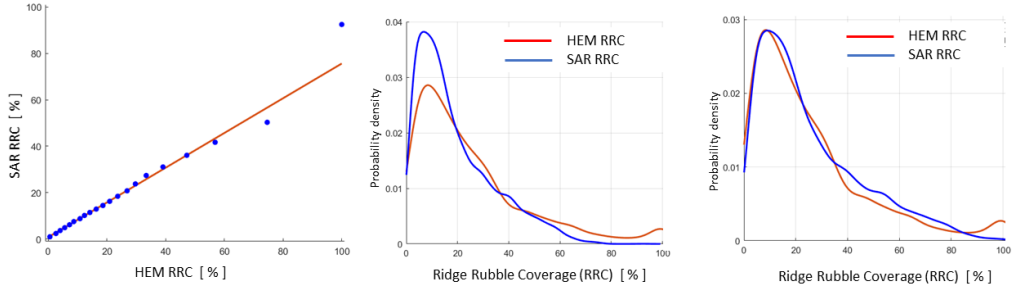

Figure 14. The quantile-quantile plot for the SAR and LIDAR data sets (left). The SAR and LIDAR RRC distributions overlaid (middle). The scaled SAR and original LIDAR RRC distributions (right).

3.2 Contextual images as ridging information

Although in SAR images from a ridged ice cover the bright returns are predominantly from ridge rubble, the step to quantitative methods has proved hard. The bright pixels do not typically connect well to ridging features. This was found here also for high-resolution SAR and was assigned to the random occurrence of favourable rubble block arrangements.

The randomness problem can partly be bypassed by the BPN approach as the ratios of BPN values do not change much even in large changes in BPP. Thus, the appearance of contextual images that enhance the ridging signature by a BPN sliding operation (Fig. **??**~~(the right panel)~~17 or Fig. 12) also does not change much. This appears more strikingly in the category versions of the contextual images (Fig. 17), which provide an application-oriented way to delineate ridged ice.

The ~~similarity of the weighted SAR RRC and original HEM RRC distributions is visually obvious.We fit the gamma distributions to both data sets. The maximum likelihood estimates for the shape parameter of the weighted SAR RRC gamma density is 1.7 and the scale parameter 15.5. The respective values for HEM data are 1.4 and 18.2. The expected values are very close to each other: 26.2% for weighted SAR RRC and 25.9% for HEM RRC. Converting the mean values to the amount of ridges yields about 13 ridges per km^2 for both data sets. For the original SAR data the estimated mean is 19.5%, i. e.about 10 ridges per km^2. Hence the HEM/SAR ratio for the expected amount of ridges per km^2 without any weighting is about 1.3~~upper panels in Fig. **??** show the 1024x1024 subimage of the high-resolution SAR indicated in Fig. **??**. (???) Both the image and its BPP 20%, $L = 21$ contextual derivative are presented as category images. However, for the BPP range from 2% (pixels with value 255) to 95%, the category image is almost identical to that in the upper right panel (mihin kuvaan viitataan? Fig02??). The same result is found for several alternative methods to generate a contextual image, like the $L = 21$ sliding block average of intensity. More strikingly, the information of the contextual image is essentially retained in different randomising transformations. In Fig. **??** in the lower left panel, the 1024x1024 image has been multiplied eight times by a random matrix that erodes the ridging signature beyond visual recognition. However, the contextual category image still emerges essentially unchanged in its main features in the right panel.

~~The SAR and HEM RRC distributions overlaid (left). The weighted SAR and original HEM RRC distributions (right).~~

~~The essential feature found in~~ The observed behaviour is due to the fact that changes in BPP, changes in method, or randomising operations on the average preserve the order of values in the contextual images. This feature is enhanced in the category versions as the flux of values across category boundaries is then relatively small. This can be studied in detail by pixel-to-pixel mapping between two contextual images. For example, mapping for the 1024x1024 subimage with $L = 21$ and BPP 20% the BPN values to matching $L = 21$ sliding intensity averages the relationship is monotonous on the average. For each BPN value, the mapped intensity averages have a normal distribution with a standard deviation in the range of 3.5–4.5. On the other hand, the widths of the ~~HEM-SAR analysis was the linear relationship between the RRC distributions from the different sources. It was also observed that if the areal extent of SAR image with fixed BPP is increased, the weighting coefficient α increases but the linear relationship holds. The increase of α likely can be attributed to the fact that the size and the location of the HEM data remains the same in all cases but the magnitude of SAR RRC grid cells decreases on average~~$70\% - 80\%$, $80\% - 90\%$ and $90\% - 100\%$ categories for the intensity average are 9, 15 and 102, respectively. Thus, the highest class, in particular, retains its delineation in this method change. More importantly, if the change in BPN values induced by a change in ambient conditions preserves the order on the average, the category images can be consistently used in the daily production of ice information.

~~If we vary BPP in the identification of potential ridge pixels from the SAR imagery, the value of α changes when the SAR image extent and the HEM data stay fixed. The validity of the linear relationship between these data sets is examined in three cases: For threshold 90 % α is 2.22, for 85 % 1.61 and in our analysis with 80 % threshold α is 1.34, that is, α increases when BPP increases and~~ The pixel block side length L affects the resolution of detail in the contextual images, and its value may be chosen to suit the context, hence the term. Including a pragmatic viewpoint, $L = 21$ of Fig. **??** and $L = 101$ of Fig. **??** (mihin kuviin viitataan?) correspond to the width and length scales of icebreaking ships so that the BPN values of contextual images provide the number of bright scatterers that the ship bow or the whole ship interacts with at a time. As BPN has been shown to be a proxy of ridge rubble coverage, the contextual images have direct pertinence to navigability. The categorised versions can be interpreted as classes of navigational difficulty, or as delineation of areas that a ship should not enter. They can be used in tactical navigation or in route optimisation that only seeks to avoid difficult ice types. More advanced route optimisation is based on physical models for the added resistance from the ridges. The ice-going speed and the probability of besetting can then be obtained in simulations that take the ice conditions along alternative tracks as input, specifically ridge density and ridge height (Kuuliala et al., 2016). As the contextual images provide only relative ridge density estimates, the ~~amount of bright pixels decreases. In all three cases the relationship between the RRC datasets is linear. The mean of the weighted SAR RRC distribution in these instances is always close to the HEM RRC mean. The range of the threshold values yielding largely linear relationship between these two datasets depend on great extent and concentration of HEM data. However, for the available datasets it is not restricted only to the BPP value used in the analysis~~scaling to true values, as well as ridge height, must be determined by other means. These may include observations from ships, measurements, or satellite data, especially ICESat-2 profiles. Another possibility is to use a ship's response, observed remotely from AIS data, to classify the contextual image signatures directly in terms of ice cover resistance (Similä and Lensu, 2018).

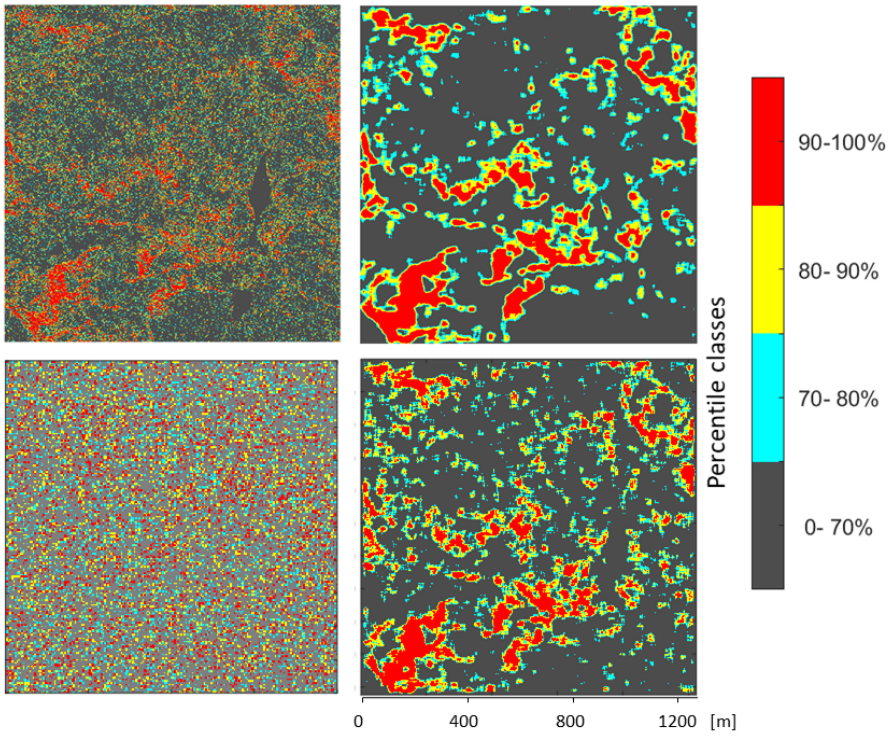

Figure 15. Results for 1024x1024 image multiplied 8 times by a random matrix. Left column: The 200x200 subimage (upper left), randomised contextual image obtained by BPP 20% and 21x21 convolution kernel (lower left). Right column: Categorisation of the original image (upper right), Categorisation of the randomised image (lower right).

~~Ridging signatures in SAR images can usually be identified by ice service experts and experienced ice navigators who also are~~

4 Discussion and conclusions

Ice charting experts are usually able to recognise the same ~~signatures in~~ ridging signatures in SAR images that have different resolutions or are taken in different ambient conditions. ~~One way to to make this observation more precise is to consider binary images that select a relatively small percentage of brightest pixels from the SAR image. The ridged ice tends to appear in these as spatial structures consisting of mostly disconnected or weakly connected pixels. Changing the percentage changes the connectivity of these pixel clouds but not their general delineation, and the same binary structures can be often identified in other SAR images with different resolutions and many different acquisition parameters. However, we note that the acquisition frequency has an important role in the ridging identification (Eriksson et al., 2010).~~

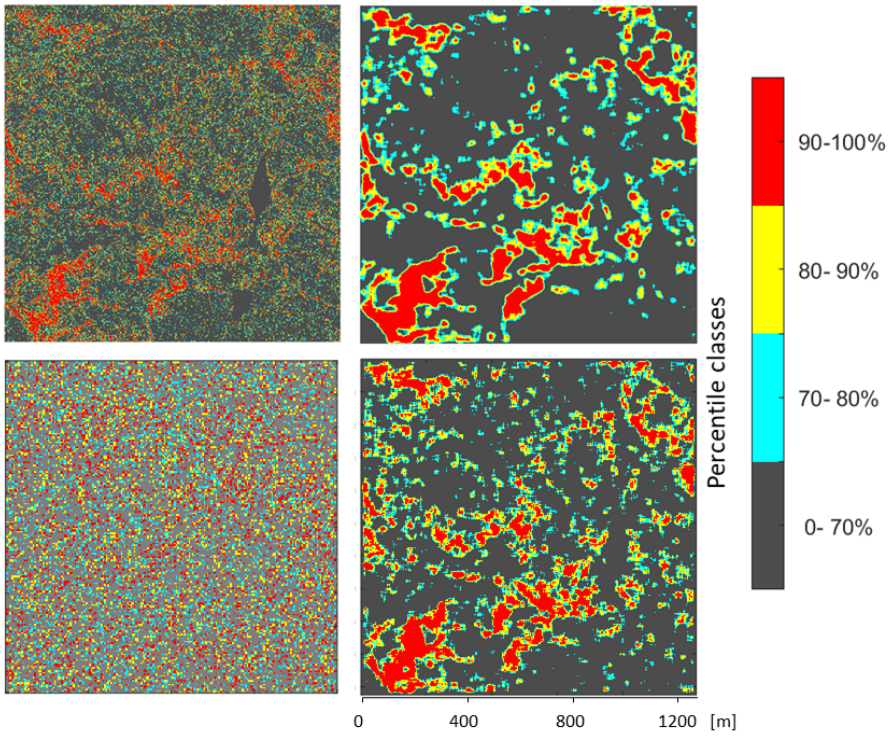

Figure 16. The contextual images (left) and corresponding category image (right) derived from the 1024x1024 subimage with BPP 20% and L=21.

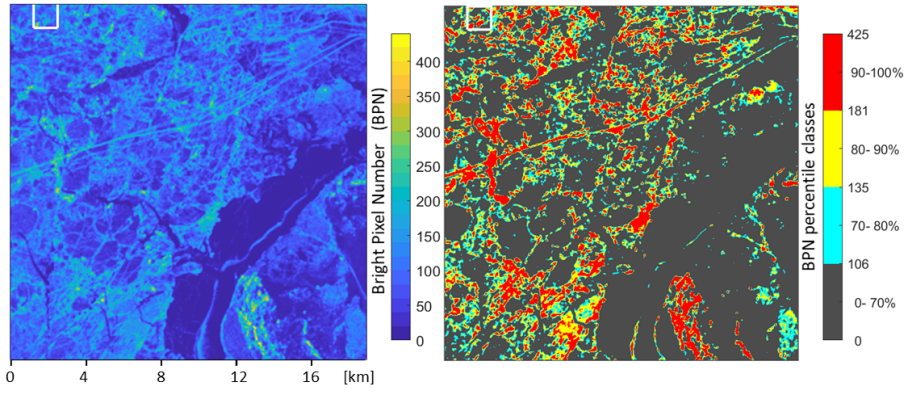

Figure 17. The contextual images (left) and corresponding category image (right) derived from the 1024x1024 subimage with BPP 20% and L=21.

~~The present approach proceeds from these observations~~ The present approach proceeded from this observation by analysing SAR images in terms of the local density of bright pixels chosen by a certain percentage (BPP). The tail intensity ~~variation, that is~~ variations, which are often relied on in SAR ice type classification approaches, ~~is~~ were left to a secondary role. The quantification is in terms of bright pixel numbers (BPN) counted in pixel blocks~~with variable side length L. The development considers first high resolution images~~. First, high-resolution images were investigated for which the bright returns can be assumed to come from individual ridge sails. ~~This also provides connection to physical studies investigating the backscattering from ridge block accumulations. The approach leads first to methods to enhance the visibility of the ridging structures and to classify SAR texture for the purposes of ice charting or ice navigation. The methods have a remarkable stability against changes in the BPP or in the intensity histogram. A more systematic foundation is then provided by a hypergeometric model for BPN distribution system that is found to apply over wide range of values for L and BPP~~A distribution model was derived and found to apply also to ridge sail numbers (RSN) determined for surface profile segments. A validation study using a medium-resolution SAR image with near concurrent ground truth data demonstrated that the method can be used to derive ridge density up to the scaling factor. This can be provided by independent observations, most promisingly by ICESat-2 surface profiles.

The ~~hypergeometric~~ distribution model was derived with a threshold process where ~~the bright pixels~~ bright pixels or ridge sail were deposited sequentially to the image canvas ~~after removing the correlations. The rate for pixels to become added to a pixel block increased linearly with the BPN of the block. This was found for a wide range of BPP and L values and provided justification for the distribution model. The value of the model parameter α, the relative strength of the Poisson component of the process, was found by fitting the model to the data by mean and variance. The model was further corroborated by a simulation where a pixel deposition process following the linear rate was shown to increase the BPP of a seed image in a realistic fashion. The linear increase rate and the distribution model were similarly found to apply to ridge sail (RSN) data in an analogical threshold process of sequential deposition of ridge sails on an 1D surface profile.~~

~~The results raise the question on the relation between the threshold process and the actual ridging process. The ongoing ridging process in a converging ice field manifests along a surface profile as appearing~~ or surface profile. The probability for the deposition to end in a certain pixel block or profile segment was proportional to the corresponding BPN or RSN value. This raises the question of the role of the physical ridge formation events that manifest as the formation of new sails to profile segments ~~, and the associated rates can in principle be determined. This can be done by sampling random profile segments of length L_i, that is, both the starting point and the orientation of the segments are random. The sample is monitored during a short time interval, and the RSN increase events in the segments and their subsegments L_j are recorded. For the following time interval this is repeated for a new sample. This minimises but does not completely remove the fact that the segments understood as lines quasi spray painted on the surface will deform in the increase events. This is less prominent for segments that are long in comparison to strains associated with ridge formation events.~~

~~Thus the hypothesis will be that the ridging as a sequential process of ridge formation events is behind the observed statistics. In this context a more common approach to spatial sail statistics in terms of~~ or as the appearance of new bright scatterers in a SAR image time series. An alternative approach to sail statistics considers sail spacings or sail-to-sail distances~~needs be considered. The formation of a~~. A new sail cuts the spacing into two, and ~~the process is analogical to a sequential fragmentation~~

process. If the if the probability for this to happen does not depend on the spacing, the spacing distribution is asymptotically lognormalas originally , as shown by (Kolmogorov, 1941). The lognormal has also been found to apply to sail spacings, in the Baltic since (Lewis et al., 1993). Conceptually, neglecting the strains, lognormal generative hypothesis of equal fragmentation probability for all spacings entails linear increase rate for larger RSN values. Thus As the RSN and the number of spacings are about equal for ridge segments, the probability that a new ridge appearing in the profile ends in a certain segment is then proportional to the RSN of the segment. This indicates that the applicability of lognormal and hypergeometric models have the same generative origin.

It is worth noting that if the 1D description of the generative process is accepted with its face value, and ridged ice thickness is described by segment averages, the thickness increase rate is higher for thicker segments. This runs counter the usual assumptions of thickness redistribution. However, the appearing of a sail to a 1D profile segment is a manifestation of a 2D ridge formation event that may extend even kilometres in along sail direction. A possible and more plausible explanation is that the initial fault triggering the ridge buildup is more likely to find its way into already damaged areas with material discontinuities and, counterpoising, stress concentrations. However, these questions are almost uncharted territory.

Although ridged ice cover lacks natural discrete units in 2D, discrete distributions can be applied in 2D to BPN values of pixel blocks. The 2D sail rubble coverage can be estimated from ridge density as in Eq. 8 and the BPN acts as a proxy for it. However, from the generative point of view the BPN is rather a proxy of RSN. If bright pixels are counted along a random line segment extending across the pixel block, the unit increase in expected pixel number in the segment corresponds to block BPN increase by some value kL. This has its physical counterpart as the along sail scale of ridge formation events exceeds the block scales of the present analysis. For this reason the BPN scale system physical origin. The lognormal has also been found to apply to sail spacings in the Baltic since (Lewis et al., 1993). Another hint of the background physical process is that the BPN statistics is parameterisable by pixel block side length L rather than block area . Also the power law decrease of the Poisson parameter α with L has exponent close to that found in RSN analysis. The power law itself suggests that the distributions have fractal support. If α is effective only within support, its value decreases with the increasing scale L of the block coverage approximating the support. Also in the simulation procedure in Section 2.3, it was found that better results were obtained by reducing the effect of α in areas with low bright pixel density.

L rather than area L^2. The length of ridge sails typically exceeds L, and thus a ridge formation event does not add bright scatterers pixelwise but as a chain crossing the pixel block. In the high-resolution SAR, it was likely that for small BPP most bright returns are from ridge rubbleand the spatial statistics was most bright pixels indicate ridge rubble. Their statistics were studied using binary BPP images, without using the intensities above the intensity threshold. No further images, and no attempt was made to interpret the intensity variations for of the bright pixels, although it may be noted they follow exponential distributionlike the ridge sail heightthat they followed exponential distribution. It was observed that the BP texture in bright pixel texture in dense ridge fields was not much different from that of ship channels that are flat rubble beds. Furthermore, very small BPP values did not delineate better ridges as curvilinear signatures which would occur if the highest intensity values are more often returns from highest ridges. All studied BPP values generated more or less the same contextual images. This suggests that the correlation between sail height and SAR intensity is weak. As no profile data were available for the

high-resolution image it It remains to be investigated whether connectedness, curvature and other measures may provide ridge height estimates.

For the medium (20 m) resolution image a regional comparison of sail and image statistics was possible and the same gamma distribution, apart from a scaling constant, was found for both. It is to be noted that the QQ plot used in the analysis is linear for gamma distributions only if the parameter α is equal for both . Thus the result corroborates the statistical model for which $\alpha = aL_j$ occurs in the gamma asymptotics. The medium resolution image was still able to capture larger individual ridging features and appeared in High-resolution SAR data provide a kind of baseline for the processing chain similarly to the high-resolution, that is, the binary BPP image consisted of clouds of mostly investigations on ridge parameter retrieval as the returns have a connection both with ground truth ridging statistics and with the backscattering models by (Manninen, 1992) and (Carlström and Ulander, 1995). The hypergeometric model provides a scale connection tool that can be used to study how lower resolution intensities relate to the pixel statistics in higher resolution matching pixel blocks. Our high- and medium-resolution images did not have the required spatiotemporal overlap, unfortunately. However, the medium-resolution image did not appear much different in binary BPP versions, which mostly consisted of disconnected pixels and the contextual image generated contextual images that enhanced the ridging features in a similar way for a wide range of BPP valuesas in the high-resolution images. Also, the simulation algorithm applied to the medium-resolution image as well as the Gamma distribution asymptotics of the hypergeometric model.

Ideal data for the present approach would consist of SAR data with different resolutions, acquisition parameters and ambient conditions over same ridged ice areas, and matching ice surface topography data from laser scanning, visual wavelength images and other methods. In the present study the ground truth data was available only for the medium resolution data with some temporal separation and approximate spatial matching. This leaves several linesof study unpursued. Perhaps the most important is the relationship of ridging signature in SAR images with a different resolutions. In the high-resolution (1.25 m) image the bright returns can be related to the presence of ridge rubble and to what is known about backscattering from block accumulations. For discussion purposes, a bright pixel in the medium resolution (20 m) image can be thought of as a $L_j = 16$ pixel block consisting of 256 high-resolution pixels. Fixing the intensity threshold for bright pixels, a certain number n_j of pixels in the block are bright returns from ridge rubble and the remaining are non-bright returns both from ridge rubble and other surface types. As these returns contribute to the aggregated return of the medium-resolution SAR, the distribution $k(n_j)$ of bright returns, Eq. 5, is certain to have pertinence to the ridging intensity variation. Further, the downscaling distribution $k(n_j|n_i)$, Eq. 3, provides connection to any longer scales $L_i > L_j$. Thus the hypergeometric scale system can provide tools for linking different SAR resolutions and for anchoring the observed intensities to the physical backscattering returns from ridge rubbleRelying on the results obtained in (Mäkynen and Hallikainen, 2004) for the scatterometer data at X- and C-band and (Dierking, 2010) for L-band SAR imagery, it can be hypothesised that the results for C-band and L-band would follow similar lines. A possible obstacle to the presented analysis occurs when the air temperature is warm enough to make the snow cover wet. As shown by (Mäkynen and Hallikainen, 2004), this essentially decreases the contrast between level and deformed ice, and thus it is uncertain whether the proposed method applies in the wet snow conditions. However, for this not to happen, any change in ambient conditions should severely overturn the order of BPN values, otherwise the persistence of contextual

category images demonstrated in Section 3.2 would prevail. In addition, higher ridges are often snow-free and less affected by wet conditions. Further studies applying matching multiplatform data with different resolutions and varying ambient conditions are needed to clarify this and other unanswered issues left open.

Data availability. The ~~laser~~ LIDAR data is available at PANGAEA under the following DOI: https://doi.pangaea.de/10.1594/PANGAEA.930545 (Haas et al., 2021).

Author contributions. Paivitys.

Competing interests. The authors declare that they have no conflicts of interest.

Acknowledgements. This work was supported by the EU, Finland, Norway, the Russian Federation ~~, and Sweden ,~~ and Sweden through the Kolarctic Cross Border Collaboration Project ~~"Ice Operations" ~~'Ice Operations' under Grant KO2100 ICEOP. Alexandru Gegiuc rectified the SAR images. Discussions with Dr Marko Mäkynen were helpful.

References

Albert, M.D., Lee Y.U., Ewe, H., and Chuah, H.: Multilayer Model Formulation and Analysis of Radar Backscattering from Sea Ice, Prog. Electromagn. Res., 128, 267-290, https://doi.org:10.2528/PIER12020205, 2012.

Breiman, L.: Random forests, Machine Learning, 45, 5–32, 2001.

Calström, A., Ulander, L. M. H.: Validation of backscatter models for level and deformed sea ice in ERS-1 SAR images, Int. J. Remote Sens., 16, 3245–3266, 1995.

~~Carlström~~Carlström, A., Ulander, L.M.H.,and Dierking, W. Radar Scattering Models and ERS-1 SAR Data Inversion for Baltic Sea Ice. In Baltic experiment for ERS-1 (BEERS). Edited by L.M.H. Ulander. Winter Navigation Research Board, National Maritime Administration, Norrköping, Sweden. Research Report 51, pp. ~~35—70~~35–70, 1994.

Calström, A., Ulander, L. M. H.: Validation of backscatter models for level and deformed sea ice in ERS-1 SAR images, Int. J. Remote Sens., 16, 3245–3266, 1995.

Carlstrom, A.: A microwave backscattering model for deformed first-year sea ice and comparisons with SAR data, IEEE T. Geosci. Remote S., 35, 378–391, https://doi.org/10.1109/36.563277, 1997.

Dierking, W. Multifrequency scatterometer measurements of Baltic Sea ice during EMAC-95, Int. J. Remote Sens., 20:2, ~~349—372~~349–372, https://doi.org/10.1080/014311699213488, 1999.

(Dierking, W. Mapping of Different Sea Ice Regimes Using Images From Sentinel-1 and ALOS Synthetic Aperture Radar, IEEE T. Geosci. Remot S., 48(3):1045–1058 https://doi.org/10.1109/TGRS.2009.2031806, 2010)

Dumitru, C.O., Datcu, M.: Information content of very high resolution SAR images: Study of feature extraction and imaging parameters. IEEE T. Geosci. Remote S., 51, 4591–4610, https://doi.org/10.1109/TGRS.2013.2265413, 2013.

Eicken, H., Gradinger, R., Salganek, M., Shirasawa, K., Perovich, D.K., ~~Leppäranta~~Leppäranta, M. (eds.): Sea ice field research techniques. University of Alaska Press, Fairbanks, Alaska, 2009.

Eriksson, L.E.B. et al. Evaluation of new spaceborne SAR sensors for sea-ice monitoring in the Baltic Sea, Can. J. Remote Sensing, 36, S56–S73, https://doi.org/10.5589/m10-020, 2010.

Fredensborg Hansen, R. M., Rinne, E., Farrell, S. L., Skourup, H.: Estimation of degree of sea ice ridging in the Bay of Bothnia based on geolocated photon heights from ICESat-2, The Cryosphere, 15:6, 2511-2529, https://doi.org/10.5194/tc-15-2511-2021, 2021.

Fritz, T., Eineder, M. (eds.): TerraSAR-X Basic Product Specification Document. TX-GS-DD-3302. Airbus DS 2013. Available online: **https://sss.terrasar-x.dlr.de/docs/TX-GS-DD-3302.pdf** (accessed on 19 May 2021).

Gegiuc, A., Similä, M., Karvonen, J., Lensu, M., Mäkynen, M., and Vainio, J.: Estimation of degree of sea ice ridging based on dual-polarized C-band SAR data, The Cryosphere, 12, 343-364, 2018.

Johansson, R. , Askne, J., Modelling of radar backscattering from low-salinity ice with ice ridges, Int. J. Remote Sens. 8, (11), ~~1667-1677~~1667–1677, 1987.

Haas, C., Lobach, J., Hendricks, S., Rabenstein, L., and Pfaffling, A.: Helicopter-borne measurements of sea ice thickness, using a small and lightweight, digital EM system, J. Appl. Geophys., 67, ~~234–241~~234–241, https://doi.org/10.1016/j.jappgeo.2008.05.005, 2009.

Haas, C., Casey, A., Lensu, M.: Safewin 2011 airborne EM sea ice thickness measurements in the Baltic Sea. PANGAEA, https://doi.pangaea.de/10.1594/PANGAEA.930545, 2021.

Hallikainen, M.: Microwave remote sensing of low-salinity sea ice. In F. Carsey (Ed.), Microwave Remote Sensing of Sea Ice, ~~361-373~~361–373. Washington D.C.: AGU, 1992.

Karvonen, J., Simila, M., and M̈ykynen, M.: Open water detection from Baltic Sea ice Radarsat-1 SAR imagery, IEEE Geosci. Remote S. Letters, 2, 275–279, https://doi.org/10.1109/LGRS.2005.847930, 2005.

Kolmogorov, A.N.: On the log-normal distribution of particles sizes during breakup process. Dokl. Akad. Nauk. SSSR, 99–101, 1941.

Kuuliala, L., Kujala, P., Suominen, M., and Montewka, J.: Estimating operability of ships in ridged ice fields, Cold Regions Science and Technology, 135, 51–61, https://doi.org/10.1016/j.coldregions.2016.12.003, 2016.

Lensu, M.: The evolution of ridged ice fields. Helsinki University of Technology, Ship Laboratory report series M, 280, 140, 2003.

Leppäranta, M., Hakala, R.: The structure and strength of first-year ice ridges in the Baltic Sea, Cold. Reg. Sci. Technol., 20:3, 295–311, https://doi.org/10.1016/0165-232X(92)90036-T., 1992.

Lewis, J. E., Leppäranta, Granberg, H. B.: Statistical properties of sea ice surface topography in the Baltic Sea. Tellus, 45 A, ~~127–142~~127–142, https://doi.org/10.3402/tellusa.v45i2.14865, 1993.

Manninen, A. T.: Effects of ridge properties on calculated surface backscattering in BEPERS-88. Int. J. Remote Sens, 13, 2469–2487, https://doi.org/10.1080/01431169208904282, 1992.

Manninen, A. T.: Surface morphology and backscattering of ice-ridge sails in the Baltic Sea. Journal of Glaciology, 42, ~~141–156~~141–156, 1996.

Melling, H.: Detection of features in first-year pack ice by synthetic aperture radar (SAR), Int. J. Remote Sens., 19:6, ~~1223–1249~~1223–1249, https:/doi.org/10.1080/014311698215702, 1998.

Mock, S. J., Hartwell, A. D., Hibler III, W. D.: Spatial aspects of pressure ridge statistics, J. Geophys. Res. 77 (30), 5945–5953, https://doi.org/10.1029/JC077i030p05945, 1972.

Mäkynen, M., Manninen, A., Similä, M., Karvonen, J., Hallikainen, M.: Incidence Angle dependence of the statistical properties of the C-Band HH-polarization backscattering signatures of the Baltic sea ice, IEEE T. Geosci. Remote S., 40, 2593–2605, 2002.

Mäkynen, M., Hallikainen, M.: Investigation of C- and X-band backscattering signatures of the Baltic Sea ice., Int. J. Remote Sens., 25, 2061–2086, 2004.

Palosuo, E., Leppŕanta, M., Seinä, A.: Formation, thickness and stability of fast ice along the Finnish coast, Styrelsen för vintersjöfarts-forskning. Research report. No.36. Finland. 19p. + appends. 1982.

Ronkainen, I., Lehtiranta, J., Lensu M., Rinne, E., Haapala, J., Haas, C.: Interannual sea ice thickness variability in the Bay of Bothnia, The Cryosphere, 12:11, ~~3459–3476~~3459–3476, https://doi.org/10.5194/tc-12-3459-2018, 2018.

~~Similä~~Similä, M., ~~Leppäranta~~Leppäranta, M., Granberg, H. B, Lewis, J. E.: The relation between SAR imagery and regional sea ice ridging characteristics from BEPERS-88, Int. J. of Remote Sens., 13:13, ~~2415–2432~~2415–2432, https://doi.org/10.1080/01431169208904279, 1992.

Similä, M, Arjas, E., Mäkynen, M., and Hallikainen, M.: A Bayesian classification model for sea ice roughness from scatterometer data, IEEE T. Geosci. Remote S., 39, 1586–1595, https://doi.org/10.1109/36.934090, 2001.

Similä, M., Mäkynen, M, Heiler, I.: Comparison between C band synthetic aperture radar and 3-?D laser scanner statistics for the Baltic Sea ice, J. Geophys. Res.- Oceans, 115, C10 https://doi.org/10.1029/2009JC005970, 2010.

~~Similä~~Similä, M. and Lensu, M.: Estimating the Speed of Ice-Going Ships by Integrating SAR Imagery and Ship Data from an Automatic Identification System. Remote Sens. 10, 1132. https://doi.org/10.3390/rs10071132, 2018.

WMO Sea ice Nomenclature, WMO n. 259 (rev, 2010), 2010.